Effect of Ionic Strength on Cellulose Nanocrystal Dispersion Viscosity and Surface Modification of Thin Film

by

Andre Tyrell Hansford

A thesis submitted to the Graduate Faculty of
Auburn University
in partial fulfillment of the
requirements for the Degree of
Master of Science

Auburn, Alabama
May 05, 2018

Keywords: Cellulose Nanocrystal, Liquid Crystal, Rheology, Microelectromechanical System

Approved by

Virginia A. Davis, Co-chair, Alumni Professor of Chemical Engineering
W. Robert Ashurst, Co-chair, Uthlaut Family Endowed Associate Professor of Chemical Engineering
Ilari Filpponen, Assistant Research Professor of Chemical Engineering

Abstract

The primary aim of this research was to explore the effect ionic strength on aqueous cellulose nanocrystal (CNC) dispersions with a range of concentrations spanning isotropic, biphasic, and liquid crystalline regimes. The CNCs used in this research were extracted from Woody biomass using sulfuric acid hydrolysis and obtained from the US Forest Products Lab. This research was partially motivated by an unusual rheological characteristic of lyotropic CNC dispersions. When viscosity is plotted as a function of mesogen concertation, lyotropic liquid crystals typically exhibit a relative maximum in the middle of the biphasic concentration regime and a relative minimum at the beginning of the liquid crystal phase. However, CNCs do not exhibit this typical rheological behavior, instead CNC dispersion viscosity simply increases with concentration. This has been attributed to the charge on the CNC and change in the overall ionic strength, and pH, with increasing concentration. This research explored the hypothesis that holding ionic strength constant across a range of CNC concentrations would result in the typical non-monotonic viscosity versus concentration curve.

Solutions of 0.01 M hydrochloric acid (HCl) and 0.1 M sulfuric acid (H_2SO_4) were added to CNC dispersions until a target ionic strength was achieved for all the dispersion concentrations. Steady shear rheology and cross-polarized optical microscopy were used to monitor the changes of the dispersion microstructure after acid addition. In general, acid addition was found to affect cholesteric pitch and viscosity. It was also found that

liquid crystal dispersions became biphasic after each acid addition; this suggests that the acid addition reduced the solvent quality. The studies using HCl addition suffered from experimental errors and were inconclusive. The sulfuric acid addition studies had less error, but failed to support the hypothesis since they did not result in the expected rheological behavior. Obtaining conclusive results was impeded by the complexity of the ionic interactions between the CNC and the added acid, and the discovery that the CNC dispersions used in this study were much more sensitive to rheological testing protocols than the CNC dispersions used in previous studies.

The secondary aim of this research was to test the feasibility of producing hydrolytically stable cellulose nanocrystals films for use in microelectromechanical systems (MEMS). Surface modification of CNC thin films included the adsorption of various chlorosilane derivatives which produced a two dimensional, self-assembled monolayer (SAM) on top of the film. Water contact angle measurements along with the time-lapsed microscopy were used to determine the hydrophobicity and hydrolytic stability of CNC thin films. The results suggest that chlorosilane, namely octyltrichlorosilane (OTS), produced water resistant CNC films when tested using a solution of OTS and hexane. However, further optimization of the application protocol is needed.

Acknowledgments

First, I would like to thank every member of the Davis Group for their support, namely Dr. Virginia Davis, Partha Saha, and Matthew Noor. Without my lab's previous findings and sincere criticism, I would not have completed this thesis. Additionally, I would like to thank my committee members, Drs. W.R. Ashurst and Ilari Filpponen, for their flexibility and open-door policy whenever I ran into trouble. Finally, I would like to thank the National Science Foundation for funding the research conducted in this thesis.

Table of Contents

List of Figures

List of Tables

Chapter 1: Introduction

The primary aim of this research was to explore the effect of ionic strength on aqueous cellulose nanocrystal (CNC) dispersions with a range of concentrations spanning isotropic, biphasic, and liquid crystalline regimes. The CNCs used in this research were extracted from woody biomass using sulfuric acid hydrolysis and obtained from the US Forest Products Lab. This research was partially motivated by an unusual rheological characteristic of lyotropic CNC dispersions. When viscosity is plotted as a function of mesogen concentration, lyotropic liquid crystals typically exhibit a relative maximum in the middle of the biphasic concentration regime and a relative minimum at the beginning of the liquid crystal phase. However, CNCs do not exhibit this typical rheological behavior, instead CNC dispersion viscosity simply increases with concentration. This has been attributed to the charge on the CNC and change in the overall ionic strength, and pH, with increasing concentration. This research explored the hypothesis that holding the ionic strength constant across a range of CNC concentrations would result in the typical non-monotonic viscosity versus concentration curve. In addition, this research evaluated literature methods for creating hydrolytically stable thin cellulose nanocrystals films [1, 2].

Cellulose has served as an industrial staple for various manufacturing purposes and can be found in paper, textile, plastic, food additive, and propellant [3]. Its unique structure is comprised of amorphous and crystalline regions which allow for cellulose to exhibit strong mechanical properties able to support the largest lifeforms on Earth. In recent years, CNCs have garnered much attention for their renewability, mechanical

properties, tailorable surface chemistry, and relatively inexpensive price point [4, 5]. The successful hydrolysis of cellulose and extraction of cellulose nanocrystals by Ranby and Ribi in 1949 ignited interest in dispersion made from this nanomaterial. In 1992, aqueous dispersions of sulfonated CNC were found to exhibit chiral nematic properties and birefringence which prompted significant research interest in the material's potential use in optical applications [6]. CNC's ability to produce selectively reflective films, due to its cholesteric structure, has the potential to be used in anti-counterfeiting coatings and other thin film CNC applications. Another interesting application for CNC is as a substitute for silicon in microelectromechanical systems (MEMS). Biomedical applications, including disposable point of care diagnostics, are one of the fastest growing segments of the MEMS industry. However, silicon MEMS are not well suited for disposable diagnostics because of the high cost and energy intensive processing which relies on the use of harsh chemicals. CNC MEMS could provide a less expensive alternative to silicon-based devices while still producing comparable mechanical properties due to CNC's high tensile strength and flexible thin film material. Regardless, of the application, there is a need to understand the behavior and rheology of aqueous CNC dispersions in order to scale production for industrial processing. In addition, understanding whether CNC's unusual rheological behavior is due to changes in ionic strength with concentration could help advance processing of other charged nanomaterials including chitin and halloysite. Herein lies the motivation behind this research on the effect of counter ions present in CNC dispersion on bulk properties.

This thesis is organized in the following manner. Chapter 2 provides relevant background information on CNC, lyotropic liquid crystal rheology and phase behavior, and MEMS fabrication. Chapter 3 provides experimental details on the materials, analytical equipment and experimental protocols. Chapter 4 describes the results particularly the effects of acid addition on the dispersion's cholesteric pitch and viscosity; it also describes unexpected challenges in obtaining accurate rheological data for the dispersions. Chapter 5 summarizes conclusions developed as a result of the work presented in this thesis.

Chapter 2: Background

2.1 Cellulose Structure and Composition

Cellulose is one of the most abundant natural polymers on the planet [7]. As a water-insoluble organic material with a relatively simple chemical structure, cellulose is utilized by a wide range of organisms from complex plant species to simpler forms of life such as bacteria, algae, and even protozoa. Cellulose is a linear polymer comprised entirely of enantiomeric β-1,4-linked anhydro-D-glucopyranose units (AGU) [8]. A repeating unit of cellulose is called cellobiose (two AGUs). Cellulose contains both crystalline and amorphous (disordered) regions, which are known to alternate in the cellulose fiber structure. Figure 1 highlights the role cellulose plays in mature plant matter such as trees, details the chemical structure of cellulose fiber and provides a simplified illustration of CNC as a building block within the cellulose fiber itself.

CNC can be extracted from biomass using various types of acid hydrolysis including hydrochloric, acetic, and sulfuric acid. All CNC have a somewhat rod-like morphology but the source affects their physical dimensions and the type of hydrolysis affects the surface chemistry [9]. Table 1 contains a list of typical CNC sources and their corresponding physical dimensions. For example, bacterial and tunicate CNC lengths range from 100 nm to several microns whereas CNC derived from wood or cotton have lengths ranging from 100 – 250 nm and widths on the order of 5 – 10 nm.

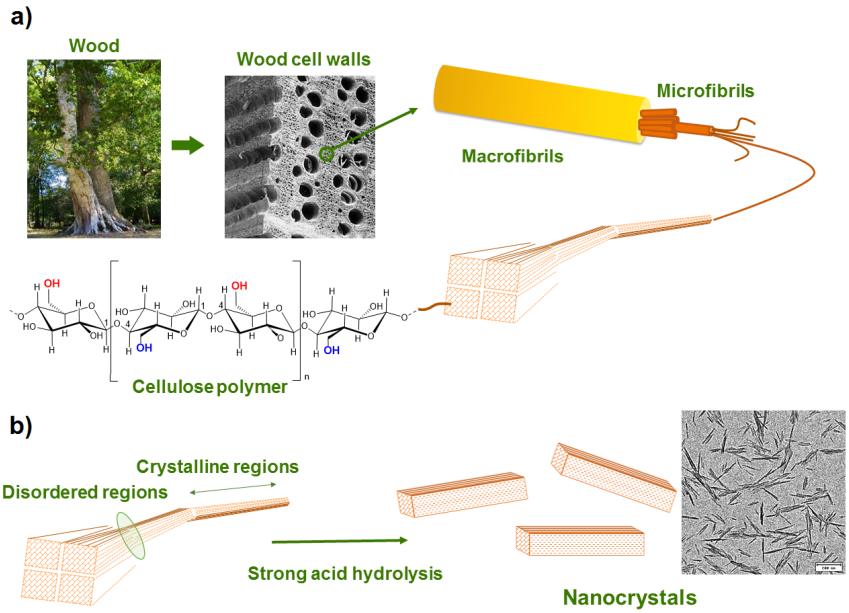

Figure 1 A) Graphic of cellulose chemical structure originating from mature biomass. B) Graphic and TEM image of CNC extracted from cellulose [9].

Table 1 Sources of cellulose nanocrystals and their respective dimensions [10].

Cellulose Type	Length	Cross Section
Tunicate	100 nm - several μm	10 - 20 nm
Bacterial	100 nm - several μm	5 - 10 nm by 30 - 50 nm
Algal (Valonia)	> 1000 nm	10 - 20 nm
Cotton	200 - 350 nm	5 nm
Wood	100 - 300 nm	3 - 5 nm

In the case of sulfuric acid hydrolysis of cellulose fiber, the exposed hydroxyl groups are partially replaced with negatively charged sulfate groups, which enables CNCs to be easily dispersed in water. Stable aqueous colloidal suspensions of cellulose crystals, isolated by sulfuric acid hydrolysis of cotton and wood pulp, were first reported

by Ranby and Ribi in 1949 [10]. The schematic in Figure 2 shows the extraction of CNC from its parent cellulose structure, highlighting the impact that sulfuric acid hydrolysis has on each nanorod once it is extracted. Hydroxyl groups on the surface of the nanocrystal are partially replaced by sulfate groups as a result of esterification [10]. When dispersed in water, dispersions of sulfuric acid hydrolyzed CNCs are classified as chiral nematic liquid crystals. This is due in part to the twisted structure of anhydroglucose units, coupled with negatively charged sulfate anions, as well as the rigidity of CNCs themselves.

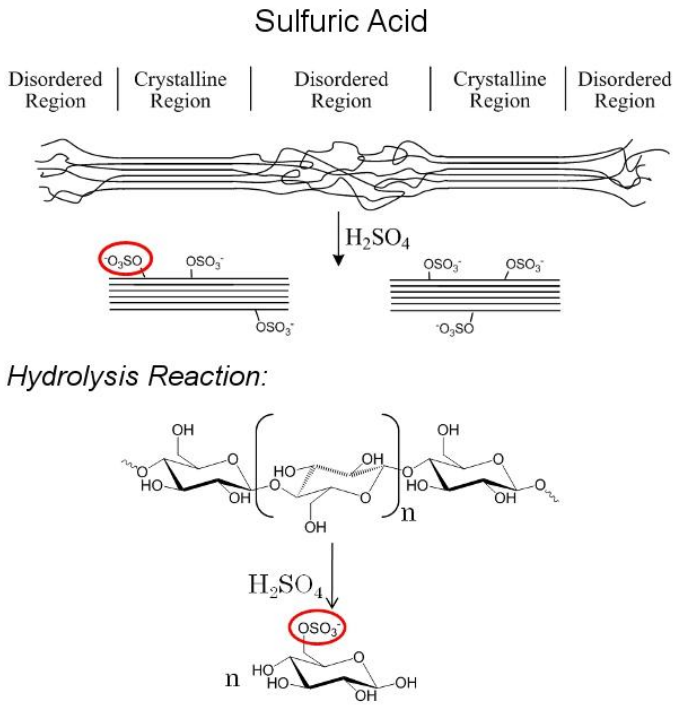

Figure 2 Sulfuric acid hydrolysis reaction producing cellulose nanocrystal with negatively charged sulfate on its surface. [11]

2.2 Liquid Crystals

Liquid crystals are a type of soft matter with long-range order similar to a crystal and fluidity similar to a liquid. Entities that form liquid crystals are classified as mesogens which must have a rigid structure and physical anisotropy (e.g. rod, disk, or platelet shapes). Liquid crystals can be classified as one of two types: thermotropic or lyotropic. Thermotropic liquid crystals (TLC) are small molecule rod-shaped or disc-shaped mesogens with a temperature dependent phase transition. In contrast, the phase transition of lyotropic liquid crystals (LLC) is dependent on mesogen concentration and are formed by higher molecular weight macromolecules [12]. Aspect ratio, the ratio of length to diameter (L/D), has the greatest influence on phase boundaries of lyotropic liquid crystals [13]. Mesogen-mesogen and mesogen-solvent interactions due to factors such as surface charge and ionic concentration will also affect dispersion phase behavior. Sulfuric acid hydrolyzed CNC dispersions can form a lyotropic liquid crystal due to both the rigid structure of the rod-like CNC and the negative surface charge caused by sulfate anions bound to each anhydroglucose unit that makes up the crystalline lattice. Less is understood about the phase behavior of CNC extracted using other means. For example, hydrochloric acid-derived CNCs have not been found to form liquid crystals; this is attributed to hydrochloric acid not producing CNCs with a strongly charged surface [10].

2.2.1 Liquid Crystalline Structure

In 1922, Georges Friedel identified three distinct liquid crystal microstructures, known as Friedelian classes, that define liquid crystal structural arrangements: smectic, nematic, and cholesteric [14]. Nematic liquid crystals display long-range orientational

order along a local director defined as *n* and short range positional order. The order parameter S describes the extent to which mesogens are aligned and ranges from 0 to 1; corresponding to complete isotropic behavior and fully aligned arrangement respectively. In Equation 2.1, θ is defined as the angle between the director n and the longitudinal axis of the rod and the angled brackets signify an average across all rods present [15].

$$\boldsymbol{S = \frac{1}{2} < 3\,cos^2\,\theta - 1 >} \qquad (2.1)$$

Smectic liquid crystals display long-range oriental order as well as long-range positional order and alignment within each layer is parallel to the director. Cholesteric liquid crystals, or chiral nematic liquid crystals, are similar to nematics in that they also possess long-range order in the direction of a local director *n*. However, cholesterics are twisted along an axis that is perpendicular to director *n*. Each full rotation along the perpendicular axis is defined as the cholesteric pitch which exhibits a finger print texture when viewed using crossed-polarized microscopy [16]. Sulfuric acid hydrolyzed CNC is classified as a cholesteric liquid crystal whose pitch is dependent on the ionic strength of the dispersion. All three types of liquid crystals are illustrated in Figure 3.

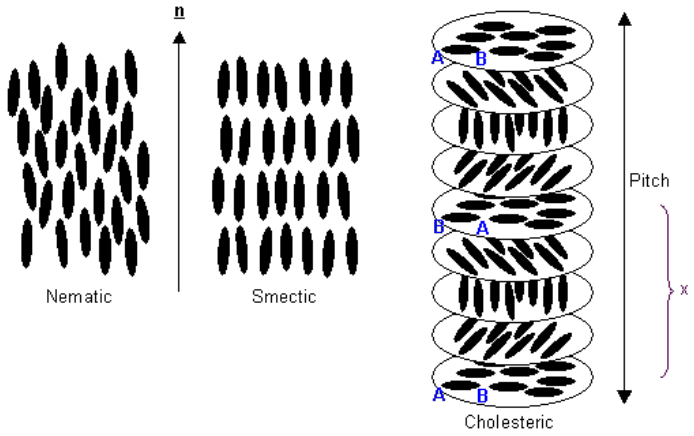

Figure 3 Three classifications of liquid crystalline structures [16].

2.2.2 Lyotropic Liquid Crystal Phase Behavior

In *The Theory of Polymer Dynamics,* Doi and Edwards outline the phase transition for rigid, rodlike polymers. Rodlike liquid crystal phases are organized into dilute, semidilute, isotropic, biphasic, and liquid crystalline regimes [17]. Figure 4 illustrates how rigid rods interact with other dispersed mesogens as rod concentration increases in a fixed volume. In the dilute regime, rods have the freedom to rotate and translate without interacting with each other. In a semidilute regime, rods are restricted in their ability to freely rotate by other dispersed rods, however, they maintain their ability to translate in the system. Progressing to an isotropic concentrated regime means there will be a loss in both translational and rotational energy, the rods can only move in the straw like volumes shown in Figure 4. Further increasing the rod concentration will force the system into the biphasic regime. The isotropic to biphasic transition concentration ϕ_i can be identified based on the first appearance of a birefringent region when the system is viewed under a cross-polarized optical microscope. This phase transition is due to the loss of rotational entropy being offset by an increase in translational entropy which minimizes the Gibbs free energy in the system. In the biphasic regime, the isotropic phase exists in equilibrium with the liquid crystalline (anisotropic) phase. Increasing the rod concentration further results in an increase in the number of liquid crystalline domains present and decreases the presence of isotropic domains until the system reaches the ϕ_{LC} concentration. At this critical concentration, no isotropic domains are present and the system is considered to be liquid crystalline. In this phase, dispersed rods are unable to freely rotate. Increasing rod concentration further restricts rod movement until a gel

concentration is reached. Dispersions of charged rods will have different critical volume factions, ϕ_i and ϕ_{LC}, when compared to their uncharged counterparts [5].

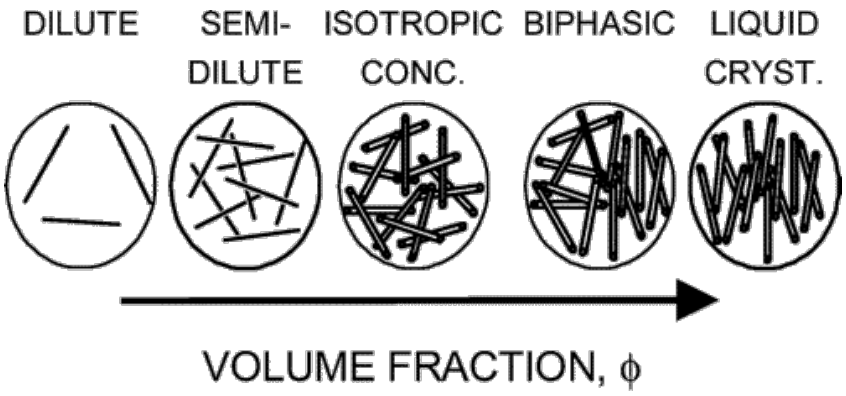

Figure 4 Monodispersed rigid rod phase regimes [18].

2.2.3 Rheological Characteristics

Unlike most other polymer solutions, which exhibit monotonic viscosity behavior with increasing concentration, lyotropic liquid crystals exhibit a viscosity peak in the biphasic phase regime when plotted as a function of mesogen concertation [19]. This same rheological behavior is seen in many other lyotropic liquid crystals [20, 19, 21]. Isotropic concentrations increase in viscosity as concentration increases until it reaches a peak in the biphasic phase when most of the system is liquid crystalline. After this peak is reached, the viscosity decreases as increasing concentration to the increasing volume fraction of the sample comprised by aligned domains. After the biphasic to liquid crystalline transition, the viscosity then increases with increasing concentration due to the lack of free volume in the dispersion. For example, the viscosity of polypeptide poly (γ-benzyl glutamate) (PBG) in solution with m-cresol peaks at 12 wt% on the viscosity versus concentration curve shown in Figure 5 [19].

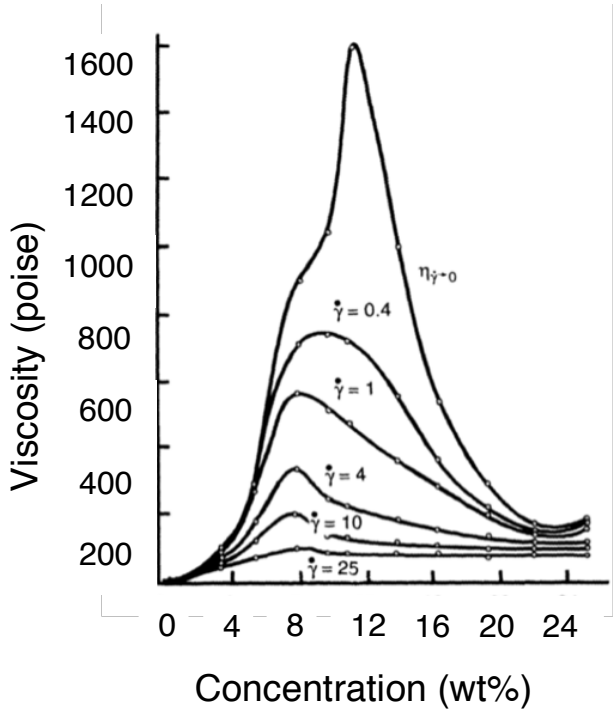

Figure 5 Viscosity vs. concentration plot of PBG in m-cresol [19].

Charged rods, such as cellulose nanocrystals, chitin, and halloysite, do not exhibit the behavior in Figure 5. Previous work by Ureña-Benavides et al. (2011) showed that CNC dispersion viscosity increases with rod concentration throughout the isotropic concentrated, anisotropic, and liquid crystalline phase regimes [22]. Figure 6 shows the behavior of CNC dispersion viscosity as a function of concentration, which in contrast to PBG in m-cresol does not show a local viscosity maximum in the biphasic region. This peculiar viscosity behavior for charged rods is generally attributed to the electroviscous effect, which is further discussed in Chapter 2.6.

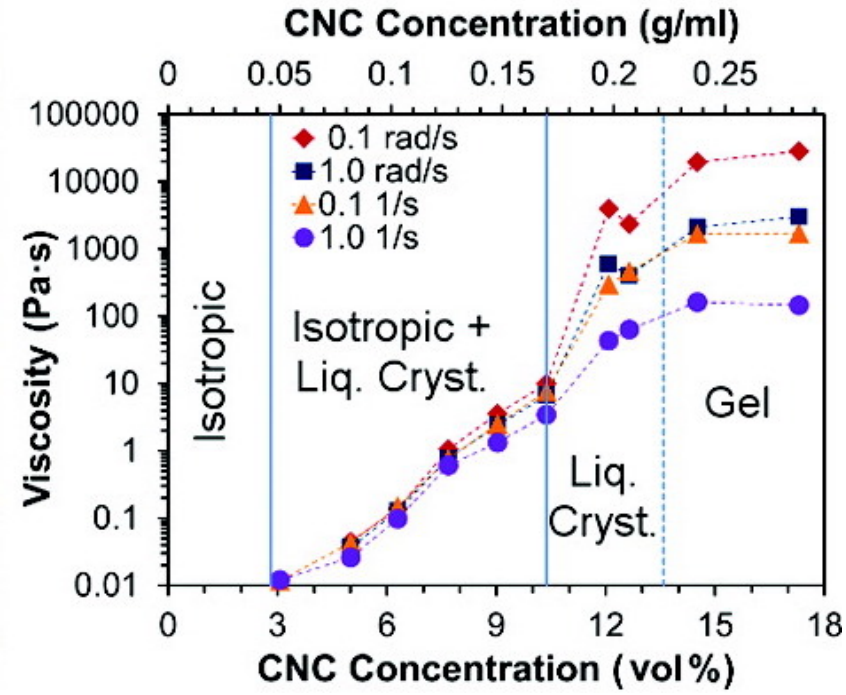

Figure 6 CNC Viscosity as a function of dispersion concentration expressed at four shear rates [22].

One additional rheological characteristic typically displayed by lyotropic liquid crystals is a three region viscosity versus shear rate curve. Figure 7 shows the flow behavior of a monodispersed, hard rod liquid crystal system first proposed by Onogi and Asada [23]. At both low (Region I) and high (Region III) shear rates, typical liquid crystals exhibit two distinct shear thinning viscosity profiles. In Region I, the dispersed rods experience tumbling within the system, which correlates to an initial shear thinning. While in Region III, individual rods align in the direction of fluid shear and orient themselves in a nematic-like fashion. At intermediate shear rates, rods experience “wagging” of the local director and display a Newtonian plateau due to vorticity alignment where viscosity is constant with increasing shear rate [24, 25]. This same flow behavior is typically exhibited

by biphasic dispersions of CNC rather than that above ϕ_{LC}, which typically display only shear thinning behavior.

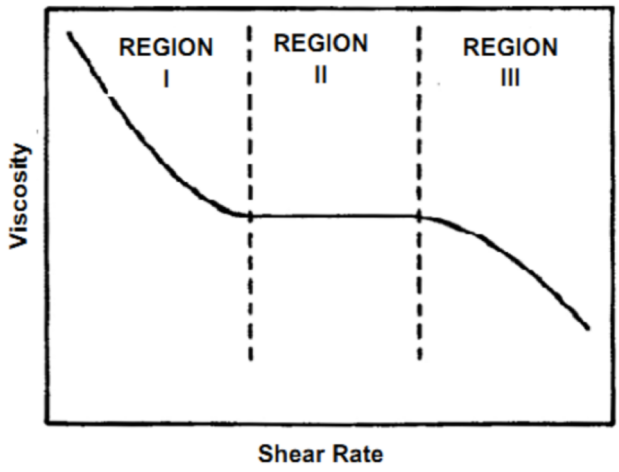

Figure 7 Onogi and Asada's three region viscosity profile for a liquid crystal dispersion [23].

2.3 Onsager Theory

Onsager's statistical mechanical theory for rigid rodlike polymers serves as the seminal underlying theory for research on lyotropic liquid crystals. His original theory considered rigid rodlike molecules with infinite length (L>>d) dispersed an athermal solvent and interacting only through excluded volume interactions, which include rod-rod and rod-solvent interactions. Phase boundary concentrations, ϕ_i and ϕ_{LC}, for a lyotropic liquid crystalline system can be predicted using Equations 2.2 and 2.3 respectively.

$$\boldsymbol{\phi_I = 3.34\frac{D}{L}} \tag{2.2}$$

$$\boldsymbol{\phi_{LC} = 4.49\frac{D}{L}} \tag{2.3}$$

Volume fraction ϕ can be calculated using Equation 2.4 where relative density ρ_{rel} is the ratio of solvent density $\rho_{solvent}$ to rod density ρ_{CNC} and w is the weight fraction of dispersed rods.

$$\boldsymbol{\phi} = \frac{\boldsymbol{\rho_{rel} w}}{\mathbf{1}+(\boldsymbol{\rho_{rel}}-\mathbf{1})\boldsymbol{w}} \tag{2.4}$$

Onsager's theory hinges on the minimization of ΔG in the Gibbs free energy equation below where ΔH is the change in enthalpy upon mixing, ΔS is the change in entropy upon mixing, and T is the temperature of the system.

$$\Delta \boldsymbol{G} = \Delta \boldsymbol{H} - \boldsymbol{T}\Delta \boldsymbol{S} \tag{2.5}$$

Since Equation 2.5 is dominated by the $T\Delta S$ term when two components are mixed, this term needs to be as large as possible as ΔG needs to be negative to obtain a stable single-phase dispersion.

While Onsager's original theory was based on monodisperse rods interacting only through hard rod repulsions, subsequent refinements have included size polydispersity and solvent quality effects [17]. The effect of the solvent quality on the phase boundaries is shown in Figure 8. Above a particular solvent quality, dispersed rods will exist in one of the three liquid crystal phase regimes: isotropic concentrated, two-phase (biphasic), or liquid crystalline regime. For poorer solvents, ϕ_I shifts to lower concentrations and ϕ_{LC} shifts to higher concentrations. Below this threshold, rods will tend to aggregate, and the suspension will no longer maintain its homogeneity.

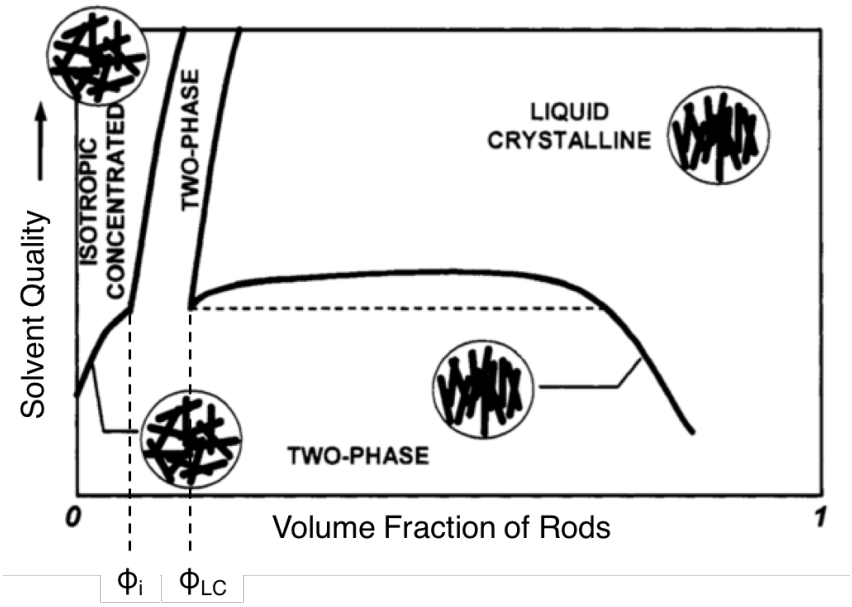

Figure 8 Phase diagram for a monodisperse rigid rod suspension [26].

2.4 Stroobants-Lekkerker-Odijik Theory

One of many variants to Onsager's theory for monodisperse hard rods was developed by Stroobants, Lekkerkerker, and Odijik (SLO). SLO theory takes into account electrostatic repulsion as well as rod orientation when calculating phase transitions, providing a realistic model for liquid crystal dispersions of charged rods. Also, Stroobants et al. address an oversight made in Onsager's original work wherein charge on a polyelectrolyte rod is not distributed evenly on the surface. Onsager's initial solution to this problem, which called for an increase in the effective diameter of the rod, did not account for rods that do not typically align due to their nonuniform charged surface [27]. Therefore, a more complex solution was accounted for in SLO theory.

$$\boldsymbol{C_i = (3.290)[(1 - 0.675h)b]^{-1}} \qquad (2.6)$$

$$C_a = (4.191)[(1 - 0.730h)b]^{-1} \quad (2.7)$$

Isotropic and anisotropic concentrations, C_i and C_a respectively, are based on the number density of rods. In Equations 2.6 and 2.7, h is the ratio of the Debye length κ^{-1} to the effective diameter D_{eff} and b is defined in defined as:

$$b = \frac{\pi}{4} L^2 D_{eff} \quad (2.8)$$

where L is the length of the polyelectrolyte in the system. This term denotes the twisting action between charged rods since electrostatic repulsion favors perpendicular orientation. D_{eff} is defined as:

$$D_{eff} = D + \kappa^{-1}(ln\, A' + 0.7704) \quad (2.9)$$

where

$$A' = 2\pi v_{eff}^2 Q \kappa^{-1} exp\,(-\kappa D) \quad (2.10)$$

In Equation 2.10, Q is the Bjerrum length which holds the value of 7.14 Å for aqueous systems at 25˚C and 7.52 Å for systems at 10˚C. D is the polyelectrolyte diameter and v_{eff} is the effective linear charge density.

2.5 Flory Lattice Theory

The primary alternative to Onsager theory is Flory lattice theory, developed in 1956. It describes the mixing interaction between a semi-flexible long chain polymer and a small molecule solvent to account for limitations associated with Onsager's original theory in 1949 [15]. Since it accounts for flexibility, Flory theory is primarily used for understanding the lyotropic liquid crystal phase behavior of rod-like polymers; however, Onsager-based theories are typically considered more relevant for rigid rod-like

nanomaterials. Flory's lattice theory takes into account all possible locations and orientations a rod could assume in a dispersion through the partition function Z. The partition function is defined in Equation 2.11 as follows:

$$\boldsymbol{Z = Z_{comb} Z_{orient}} \tag{2.11}$$

where

$$\boldsymbol{Z_{comb} = \frac{1}{n_p!} \prod_{j=1}^{n_p} v_j} \tag{2.12}$$

$$\boldsymbol{Z_{orient} = \prod_y (\frac{\omega_y n_p}{n_{py}})^{n_{py}}} \tag{2.13}$$

The combinatory term for lyotropic liquid crystals, expressed by Equation 2.12, explains the loss in rotational entropy rods in the lattice experience as rod concentration increases and a phase change occurs in the system. In Equation 2.12, j is an additional rod being added to the system or lattice, n_p is the number of identical rods currently placed in the lattice, and v_j is the number of possible positions rod j can occupy [15]. Deconstructing the orientational term in Equation 2.13, y signifies the disorientation of a rod in relation to the local director, n_{py} is the number of rods at a given angle of orientation from the director, and ω_y is the angle of disorientation for a single misaligned rod in the lattice.

Flory's lattice model is useful in elucidating the critical volume fraction need to produce a metastable, or partially ordered, solution. His model employs v_p^* to signify the critical volume fraction needed to produce such a solution based on the axial ratio, χ

calculated by taking a ratio of the contour length and persistence length, using Equation 2.14:

$$\boldsymbol{v_p^*} = \frac{\mathbf{8}}{\boldsymbol{x}} - \frac{\mathbf{16}}{\boldsymbol{x^2}} \tag{2.14}$$

Plotting $(lnZ\text{-}lnZ_{y=1})$ against rod misalignment $(\bar{y}/x)$ and using Equation 2.14 to determine the volume fraction needed to produce a metastable solution helps determine ϕ_i for liquid crystals. The term $(lnZ\text{-}lnZ_{y=1})$ normalizes the ln function of the Z partition in relation to a system with perfectly aligned rods. Partition function Z describes the ability for rods within a system to reach an equilibrium point and is considered in calculating the enthalpy upon mixing two phases in Equation 2.15 and subsequently Equation 2.16.

$$\Delta \boldsymbol{H_{mix}} = \boldsymbol{Z}\Delta \boldsymbol{w_{12}} \boldsymbol{n_1} \boldsymbol{n_2} \tag{2.15}$$

$$\Delta \boldsymbol{G_{mix}} = \boldsymbol{\Delta H_{mix}} - \boldsymbol{T\Delta S_{mix}} \tag{2.16}$$

In the equations above, ΔH_{mix} is the change in enthalpy upon mixing, Δw_{12} is the change in bonding energy, and $n_1 n_2$ is the product of the molar components within the lattice. Since ΔG_{mix} needs to be negative for a solution to favor homogeneity, Flory lattice theory helps explain how ΔH_{mix} decreases upon further addition of a dispersed nanorod to generate a stable system.

2.6 Electric Double Layer

The continuous increase in CNC dispersion viscosity with increased rod concentration is generally attributed to charged ions on their surface [28]. Due to the negatively charged sulfate group on the CNC surface, positively charged counterions present in the system surround the negatively charged dispersed rods and form an ion dense Stern Layer [29, 30, 31]. An electrical potential can be measured between the

surface of the charged rod and the slipping plane, which lies between the compact Stern Layer and diffuse layer [31]. A schematic of the Stern and diffuse layers, i.e. the electric double layer (EDL), is presented in Figure 9.

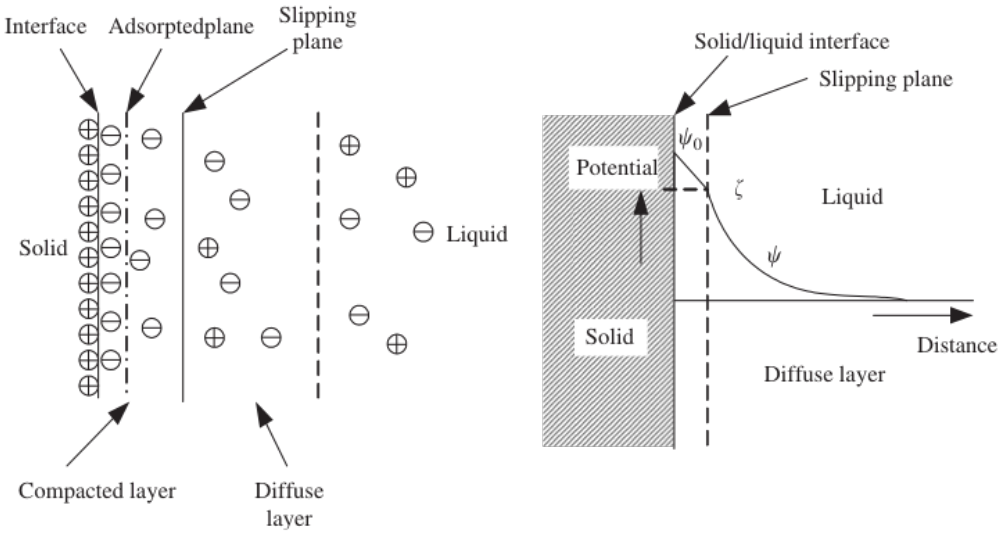

Figure 9 Schematic of EDL structure (left) depicts concentration of ions in dispersion near CNC surface and electrostatic potential diagram (right) illustrates charge depletion with increasing distance from rod surface. [31]

In 2012, Zuo et al. studied the effect of an electric double layer on thermal elastohydrodynamic lubricants. The team found a positive correlation between film temperature and the characteristic thickness of the electric double layer [17]. Furthermore, they highlight the impact that electrolyte concentration and temperature have on the characteristic thickness of the EDL κ^{-1}.

$$\boldsymbol{\kappa} = \left[\frac{8\pi n e^2 z_e^2}{\varepsilon k_B T}\right]^{0.5} \tag{2.17}$$

Equation 2.17 calculates the reciprocal Debye length where n is the number concentration of ions in bulk solution (m^{-3}), e is the elementary protonic charge (1.602 X 10^{-19} C), z_e is the electrovalence of the ion bound to the solid surface, ε is the absolute

dielectric constant of the fluid (F/m), and k_B is the Boltzmann constant (1.38 X 10^{-23} J/K). Given this correlation, one can conclude that ions with a weak electrovalence will produce a thicker EDL; i.e. increase the value of κ^{-1}. Furthermore, an increase in temperature will also increase the characteristic thickness of the EDL. Although counterintuitive, a thicker double layer led to a decrease in lubricant viscosity. Figure 10 plots characteristic EDL thickness and dimensionless electro-viscosity as a function of temperature [30].

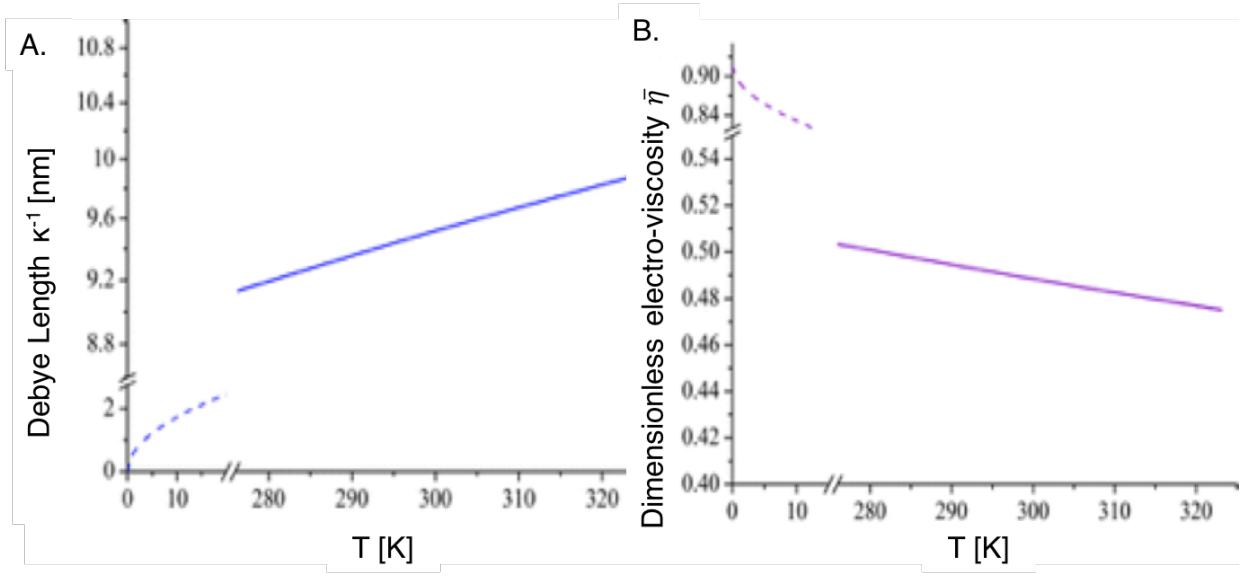

Figure 10 A) Plot of characteristic EDL thickness as a function of temperature. B) Dimensionless electro-viscosity plot as a function of temperature [30].

The reciprocal Debye length becomes important when one calculates the apparent viscosity η_a, defined by Equation 2.18. In Bai and colleague's adaptation of Zhang's initial calculation of apparent viscosity, the team includes the influence of film thickness on the potential streaming gradient.

$$\boldsymbol{\eta_a = \eta + \frac{3\varepsilon^2\zeta^2}{4\pi^2\kappa^{-2}h^4\lambda}\left[\frac{(cosh(\kappa)-h-1)^2}{sinh(\kappa)-h} - sinh(\kappa) - h + \kappa - h\right]^2} \qquad (2.18)$$

In the equation above, the second term on the right-hand side calculates the electro-viscous force, η_e. This force is inversely proportional to film thickness h and

directly proportional to the zeta potential, ζ. As a result, the electric double layer has a more significant impact on determining apparent viscosity for thinner films and reaches a peak value for films with a thickness five times that of κ [30]. After this maximum thickness, the influence of the EDL on apparent viscosity diminishes significantly. In the model, Zuo et al. suggest that the double layers of the two solid, lubricated surfaces overlap and become thinner which results in a viscosity decrease below 5κ.

Although this theory addresses lubrication between surfaces and the effect of EDL diminishes with increasing film thickness, a decrease in CNC dispersion viscosity upon acid addition would support the notion that these same principles may apply to hard rods dispersed in an electrolyte-rich aqueous medium. Since κ appears in the denominator of the second term in Equation 2.18, and assuming this model holds true for charged rods in dispersion, an increase in κ would lead to a decrease in apparent viscosity η_a. If nothing else, a decrease in CNC viscosity would warrant further experimentation to conclusively determine whether dispersion of CNCs behave similarly to lubricant at a gap height of 5κ.

2.5 Micro-electromechanical Systems (MEMS)

Micro-electromechanical systems (MEMS) integrate mechanical devices with electrical components that can transmit a response signal to a receiver [2]. Some MEMS devices such as accelerometers and pressure sensors have become ubiquitous in twenty-first century products, ranging from smartphones to airbag deployment systems. However, other MEMS applications have failed to achieve the same spike in commercialization due to the lack of standardized packaging and shortcomings that pertain to physical limitations such as stiction, surface work of adhesion, etc. [2, 32].

MEMS device fabrication continues to be in high demand due to the expansion of the Internet of Things (IoT), a category of consumer products which have the ability to communicate across a wireless network. One industry in particular that stands to gain from the advancement of MEMS integration is the biomedical industry, particularly in expanding the availability of quality biomonitoring devices to those who live in areas lacking affordable and reliable healthcare infrastructure. Herein lies the motivation behind developing a CNC based MEMS platform with the potential to offer an alternative to silicon devices at a less expensive price point.

The device fabricated in this research was a cantilever beam array, to be used in protein immobilization for biosensing devices. Cantilever beams have a springboard shape with one end that is attached to the substrate and a free end that can flex in the presence of a targeted immobilized protein. Individual cellulose nanocrystals have a bending strength of 10 GPa and a Young's modulus of 150 GPa, these are comparable mechanical properties to those of silicon whose Young's modulus is on the order of 165 GPa [33, 34]. Because of these properties, CNC is being explored as an alternative material to use in the fabrication of micro-cantilever arrays.

2.6 Photolithography

Photolithography, the process used to fabricate MEMS devices using thin film CNC, is commonly used in the microelectronics industry. The process begins by coating a substrate, in our case a single crystalline silicon wafer, with a photoresist layer. A positive photoresist, AZP4620, was chosen to build device anchor sites. The photoresist layer is exposed to UV light for 30 seconds under a chrome anchor mask on a quartz

slide. However, the exposure time can vary based on the photoresist chosen. The exposed resist is then submerged in a developer solution consisting of a 3:1 deionized water to AZ400K for 90 seconds. This protocol is repeated for the device layer after a thin film of CNC is applied to the silicon wafer. Devices are released from the substrate using carbon dioxide in a critical point drier.

2.7 Self-Assembled Monolayer (SAM)

Self-assembled monolayers (SAM) are two-dimensional structures, typically surfactant molecules, adsorbed onto a desired substrate [35]. SAM formation can be an alternative to fluid phase processing as a means of achieving hydrolytically stable films without altering dispersion composition. Fluid phase processing changes the microstructure of the fluid phase by introducing additives, in our case maleic acid and sodium hypophosphite, to achieve hydrolytically stable films. SAM formation is a post process application that is applied after producing thin CNC films and can be applied in either the gas or liquid form. Since most industrial processes are more cost-effective when liquid alternatives are available, silane SAM application has the potential to be easily scaled for industrial application.

Chlorosilane SAM application utilizes the polarity difference between the polar head of the molecule and nonpolar carbon tail to create a hydrophobic boundary between the target substrate and the surrounding environment. SAM coating requires the hydrolysis of a precursor chlorosilane before substrate attachment and is aptly described by Equation 2.19 in which 3 HCl molecules are produced for every silanol as a product of the hydrolysis [2].

$$RSiCl_3 + 3\,H_2O \rightarrow 3\,HCl + RSi(OH)_3 \quad (2.19)$$

Only chlorosilanes are tested in this study and will, therefore, follow the same chemical reaction during hydrolysis. This step is followed by a condensation reaction that adsorbs silanol molecules to the substrate surface and subsequently links adjacent silanol molecules and produces water as a byproduct. Due to polarity differences between the head and tail of chlorosilane molecules, the formation of a self-assembled silane monolayer is self-limiting and uniform. Figure 11 illustrates the attachment and arrangement of a chlorosilane at a substrate surface. The use of various silane species in the formation of SAM is of interest because they are highly tailorable at both ends of the molecule and form densely packed monolayers with minimal defect regions [35]. The pace at which monolayer formation takes place is dependent on the reaction temperature. Furthermore, reaction threshold temperature was found to be a function of chain length, in that, longer silane chains have a higher reaction threshold temperature. This correlation proved to be of great importance in determining optimal reaction conditions.

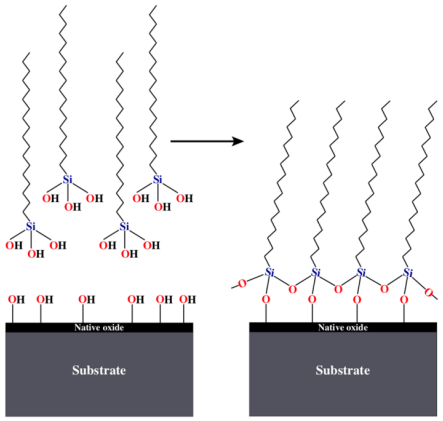

Figure 11 Schematic depicting the attachment of trisilanol to a silicon dioxide substrate. Not shown is the hydrolysis of the octyldecyltrichlorosilane precursor [2].

Chapter 3: Experimental

3.1 Cellulose Nanocrystal Dispersion Preparation

Cellulose nanocrystals used in this research were purchased from the US Department of Agriculture Forest Product Lab (Lot numbers 2015-FPL-CNC-077 and 2016-FPL-CNC-098) and supplied by the University of Maine. The mass concentration of CNC for the 2015-FPL-CNC-077 as received batch was 11.2 wt% and the degree of sulfonation was 0.94 wt% sulfur on dry CNC. The degree of sulfonation and mass concentration for the 2016-FPL-CNC-098 as received batch was 0.95 wt% sulfur on dry CNC and 12.1 wt% dry CNC, respectively.

Atomic force micrographs of diluted CNC samples from both stock dispersions are presented in Figure 12. Both images show some aggregates which could have been present in the original sample or the result of sample preparation and drying. The greater number of aggregates in the 2016-FPL-CNC-098 image are believed to be the result of drying and imaging protocol. Size estimates for each batch are based on average dimensions for individual CNC rods, approximately 100 rods for 2015-FPL-CNC-077 and 30 rods for 2016-FPL-CNC-098. The average length and height for 2015-FPL-CNC-077 were 157 and 5.21 nm, resulting in an average aspect ratio of 30.1 nm. For lot 2016-FPL-CNC-098, the average lengths and heights were 98.6 and 6.2 nm resulting in an average aspect ratio of 15.9 nm. It should be noted that CNC are not truly cylindrical, and their width is greater than their height. However, the height measured by AFM is often used in aspect ratio calculations [13]. While more measurements would be needed to be conclusive, the average lengths of lot 2015-FPL-CNC-077 suggests that this batch has a

significantly higher aspect ratio than 2016-FPL-CNC-098 which would result in the formation of a liquid crystal dispersion at a lower concentration of CNC [13].

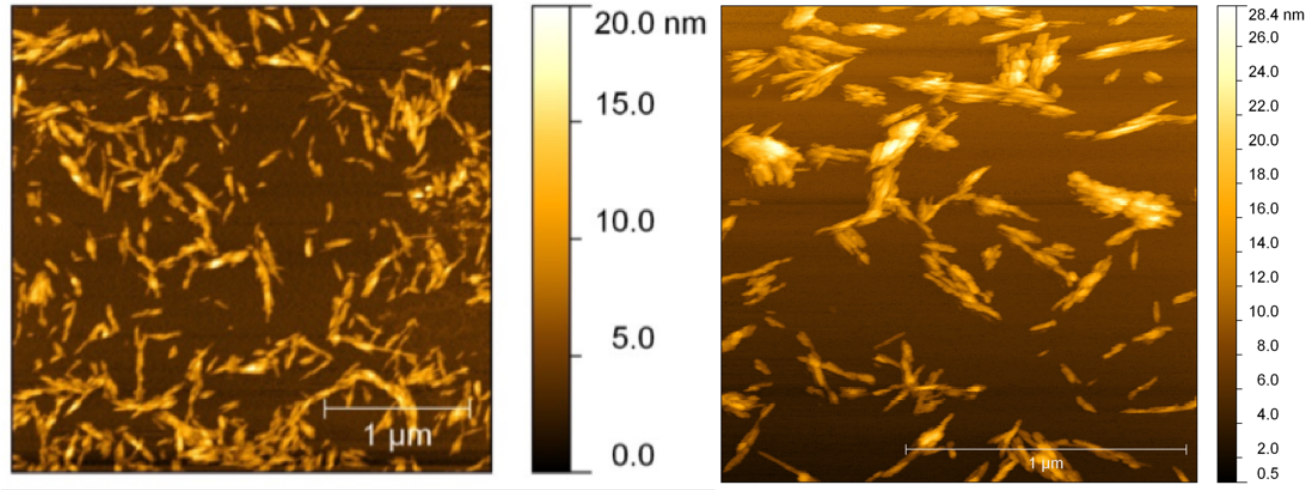

Figure 12 Atomic force micrographs of FPL-CNC. (Left) Image taken by Partha Saha. Lot number 2015-FPL-CNC-077. Average Length: 157 nm Average Diameter: 5.21 Aspect Ratio: 30.1 (Right) Lot number 2016-FPL-CNC-098 Average Length: 98.6 nm Average Diameter: 6.2 nm Aspect Ratio: 15.9

The US Forest Products Lab hydrolyzes strip-cut wood pulp using sulfuric acid (64 wt%) in a 60 minute hydrolysis process which is neutralized by using NaOH to a solution with low ionic strength. Insoluble cellulose crystals are separated after passing through a filtration system to produce a gel slurry which can be stored in a refrigerated environment [5]. The sulfuric acid hydrolysis process results in partial replacement of the surface hydroxyl groups with negatively charged sulfate groups. This esterification reaction allows CNC to be easily dispersed in water. The final gel product had a relatively high ionic strength and low water content which helped stave bacterial growth and simultaneously extended the product's shelf life [36]. All dispersions were prepared based on the CNC concentration of mass; all results are given based on volume because, as described in Chapter 2.2.2, both rheological properties and lyotropic phase transitions are a function of the volume of the samples occupied by the mesogen.

For each concentration tested, a 30 mL dispersion was prepared using ultra-pure deionized water, vortex mixed for approximately 10 minutes, and allowed to bottle roll over night to ensure uniform dispersion. Equation 2.4 was used to convert CNC mass fraction w to volume fraction ϕ where ρ_{CNC} *and* $\rho_{solvent}$ are 1.60 and 0.997 g/mL, respectively. Optical microscopy images, conductivity, and pH measurements of the resulting dispersions were obtained prior to adding H_2SO_4 or HCl to investigate the effects of acid addition.

3.2 Ion Exchanged Cellulose Nanocrystals

Unlike CNC prepared in house form the sulfuric acid hydrolysis of cotton, used in many previous works including Ureña-Benavides et al [22], CNC from the US Forest Products Lab has Na^+ instead of H^+ as the counterion. Since sodium has a lower ionization energy than hydrogen, it is unable to as easily pull free electrons in dispersion and thus exhibits weakened chiral nematic interaction when diluted to a biphasic or anisotropic concentration [37]. Sodium chlorite and sodium hydroxide are commonly used in FPL's manufacturing process to remove residual color that may be found after hydrolysis is performed and to neutralize sulfuric acid that may still be present after reverse osmosis to remove excess water [5]. In an attempt to directly compare the effects of the counterion, ion exchange was attempted on a portion of Lot 2015-FPL-CNC-077. Specifications for selecting column dimensions and protocol for completing the procedure were adapted from Beck et al. [38].

A 500 mL batch of 0.31 vol% CNC dispersion was passed through a Burette containing Dow Marathon C exchange resin at a flow rate of 3 mL/min. An additional

Burette was used to regulate the throughput of CNC. The first 40 mL of ion exchanged CNC dispersions were discarded to ensure CNC in the dispersion sample had equal exposure to ion exchange resin. Once the ion exchange process was completed, excess water present in the dispersion was slowly evaporated using a Barnstead Lab-line Multi-Purpose Rotator at ambient temperature and pressure.

3.3 In-House Cellulose Nanocrystal Isolation from Cotton

To prepare cellulose nanocrystals without sodium cations present in the EDL, CNC was isolated from Whatman Ashless Filter Aid using a well-established batch process sulfuric acid hydrolysis [10, 39]. The protocol called for 17 mL of 64 wt% H_2SO_4/g of cotton cellulose, which amounted to 255 mL of sulfuric acid for a 15 g batch of cellulose. A water bath, maintained at 45˚C, surrounded the reaction vessel while the cotton filter aid/sulfuric acid slurry was agitated by an overhead mixer for 50 minutes. Once hydrolysis was complete, the reaction was quenched using 255 mL of chilled deionized water. The mixture was then separated into 30 mL tubes and centrifuged at 24,400 RCF, or approximately 42,300 xg, for four 5 minute cycles. Between each cycle, the supernatant was decanted, the cellulosic gel at the bottom of the tube was redispersed in deionized water, and the suspension was vortex mixed to maintain homogeneity prior to the subsequent centrifuge cycle. After washing the isolated CNC to remove impurities and residual sulfuric acid, dialysis was performed until the bath's pH remained constant; a process that took eleven days in total. Dialysis water was replaced twice daily to maintain an ion concentration gradient that favored diffusion to the bath. Once completed,

concentrated CNC was tip sonicated for 35 minutes, pulsing at 60% amplitude for 7 minutes with a 2-minute rest period between each pulse.

Excess water present in the aqueous nanocrystal dispersion was evaporated at ambient temperature and an orbital shear mixer maintained agitation. Despite constant agitation, isolated CNC began to flocculate overnight. Both tip and bath sonication were used to break flocs, however, the dispersion was unstable when left to evaporate for an extended period. Although the pH of the in-house isolated cotton CNC was considerably higher than that of the counterion exchanged CNC batch, 5.14 and 2.90 respectively, the two dispersions behaved similarly. Flocculation occurred almost spontaneously for the in-house isolated batch of cotton derived CNC.

Previous work by Haywood and Ureña-Benavides et al. used the same protocol for CNC isolated from cotton and resulted in uniform dispersed nanocrystal dispersions [22, 40]. Therefore, problems with CNC aggregation encountered in this study was most likely due to improper or another procedural error. However, due to time constraints, the in-house preparation method for isolated cotton cellulose nanocrystals was not pursued.

3.4 Characterization of Cellulose Nanocrystal Dispersions

The dispersions were characterized using cross-polarized optical microscopy, steady shear rheology, and thermogravimetric analysis. A limited amount of oscillatory rheology data was also obtained to determine the viscoelastic range and identify an operating temperature to slow solvent evaporation. These tools provided useful insight on the change in CNC dispersion microstructure after the addition of HCl and H_2SO_4.

Cross-polarized optical images were used to measure pitch length for dispersion concentrations that exhibited birefringent anisotropic domains.

3.4.1 Cross-Polarized Optical Microscopy

Images of CNC dispersions were taken using cross-polarized optical microscopy on a Nikon Eclipse 80i optical microscope equipped with an LU Plan Fluor 20X/0.50 NA objective lens with 2x optical magnification. A schematic of the microscope used in this study is presented in Figure 13. Equation 3.1 was used to determine the optical resolution where NA is the numerical aperture of a particular lens and λ is the wavelength of light, typically 550 nm. Therefore, the optical resolution in the images used in this study was 550 nm.

$$\boldsymbol{r = \frac{\lambda}{2NA}} \tag{3.1}$$

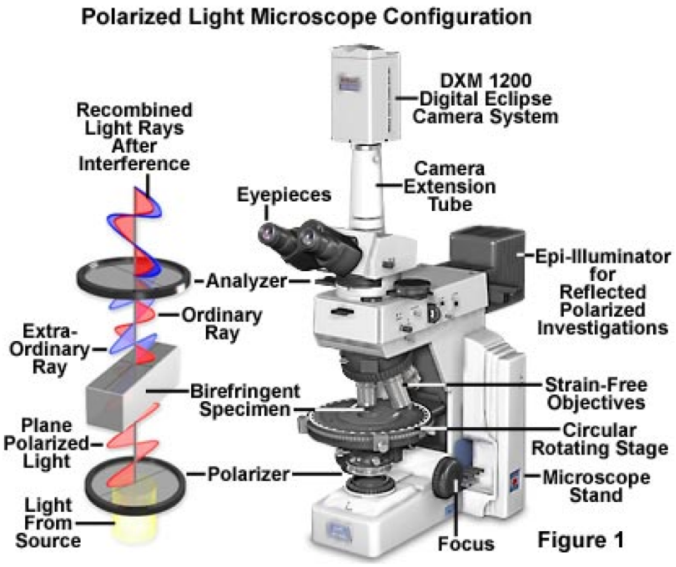

Figure 13 Schematic of Nikon Eclipse 80i optical microscope used to image CNC dispersion samples for pitch measurements [41].

Cross-polarized optical microscopy enables the detection of birefringence and was used to estimate ϕ_i, the lowest concentration with any birefringent domains, and ϕ_{LC},

lowest concentration at which no isotropic domains existed. In addition, microscopy can be used to visualize the change in microstructure that often results from ϕ_{gel}, the transition from a liquid crystal to a gel. Birefringent materials or domains have two refractive indices which are optically visible when place between a polarizer and an analyzer. When aligned, the optical intensity of birefringent domains present in CNC dispersion changes based on the degree of stage rotation in relation to the polarizer's optical axis [42]. In contrast, isotropic dispersions are not birefringent; they appear black at all rotations relative to the polarizer.

Samples for imaging were placed on a glass microscopy slide using a drawn glass stir rod, a 120 μm spacer, and a cover slip sealed with a nail polish. Chiral nematic pitch measurements were made using ImageJ post-processing software. Pitch length correlates to the distance spanning two white lines and two black lines of the fingerprint texture seen in microscopy images.

3.4.2 Rheology

Steady shear rheological measurements were taken using an Anton Paar MCR301 rotational rheometer. Rheology was conducted at 25˚C, and solvent evaporation was mitigated using an evaporation hood. Water was placed around the CNC dispersion sample during tests to increase the humidity of the air inside the evaporation hood.

Once loaded, dispersions were typically sheared at a rate of 0.001 s^{-1} for 15 minutes in an effort to eliminate any loading-induced artifacts were present. A step rate test was then performed at a shear rate of 0.01 s^{-1} to determine the amount of time needed for the sample's viscosity to become constant at that shear rate. Finally, a flow curve was

generated to obtain viscosity as a function of shear rate, 0.01 s-1 to 100 s^{-1}. The majority of measurements used for data analysis were carried out using 50 mm diameter parallel plate (PP50) and cone and plate (CP50) geometries. Some data was also acquired using the Mooney-Ewart geometry. Data that did not meet the instrument's minimum torque requirement of 0.1 μNm were not included in the analysis and data plots. Amplitude sweeps at a fixed frequency of 10 s^{-1} were repeated within the linear viscoelastic region for up to 2 hours to determine how long the sample microstructure was stable. The primary concern was changes in the sample microstructure that could result from evaporation. Surprisingly, longer stability times were found at 25˚C than 10˚C. Schematics of the fixtures used in this study are shown in Figure 14.

In the early stages of this research, rheological measurements were taken with 25 mm diameter parallel and cone and plate geometries. Since rheological properties are intrinsic material properties, they should not be dependent on the measurement fixture used. It is standard practice to measure rheology samples on multiple types of fixtures to ensure that the measured data is not the result of any fixture related artifacts. Such artifacts can result from slip, confinement, edge fracture, and evaporation, and improper loading [43]. Such artifacts were not observed during data acquisition for Ureña-Benavides et al. [22, 44]. However, in the case of the CNC used in this research, fixture related artifacts were observed by multiple people. These results are discussed in more detail in Sections 4.1.1 and 4.1.2. Unfortunately, rheology data for HCl addition experiments were taken using both diameter fixtures and the discrepancy was discovered

after CNC from the lot used for that portion of the research (2015-FPL-CNC-077) was exhausted.

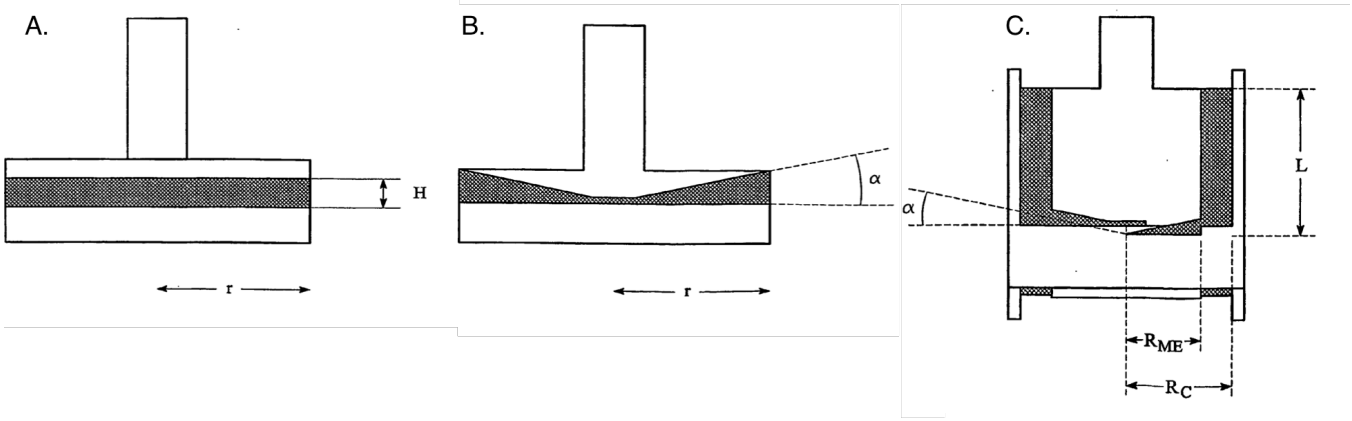

Figure 14 Rheometer fixture geometries used to measure steady shear viscosity. **A**. PP50 with r = 50 mm and variable H from 0.5 to 1 mm **B**. CP50 with α = 2.018˚ and a cone truncation of 52 μm **C**. ME21 with α = 3.18˚ R_{ME} = 10.5 mm R_C = 11.1 mm and L = 51.95 mm

Newton's law of viscosity (Equation 3.2) states that, for a fluid under shear, stress τ will be proportional to the velocity gradient in the y direction, where η is the coefficient of viscosity.

$$\boldsymbol{\tau_{yx} = \eta(\frac{dv_x}{dy})} \tag{3.2}$$

For non-Newtonian fluids, such as CNC dispersion, η is a function of the velocity gradient. Solving for η in Equation 3.2 gives the ratio of shear stress to the velocity gradient, or shear rate $\dot{\gamma}$. Since viscosity is a material property, Newton's law is used to calculate viscosity regardless of the fixture chosen. However, shear rate and stress calculations are dependent on fixture geometry and surface area. Equations 3.3 and 3.4 are used to calculate shear stress and shear rate using a cone and plate fixture.

$$\boldsymbol{\tau_{\theta Z}} = \frac{\boldsymbol{3M}}{\boldsymbol{2\pi R^3}} \tag{3.3}$$

$$\boldsymbol{\dot{\gamma}} = \frac{\boldsymbol{\Omega r}}{\boldsymbol{r sin(\beta)}} = \frac{\boldsymbol{\Omega}}{\boldsymbol{\beta}} \tag{3.4}$$

In Equations 3.3 and 3.4, M is torque generated by the rotation of the fixture, R is the radius, Ω is the angular velocity, and β is the truncation angle of the cone. For a truncation angle less than or equal to 0.1 rad, the simplification $\sin(\beta) \approx \beta$ can be substituted.

Viscosity data collected from a parallel plate fixture can be calculated using the same shear stress to shear rate ratio above. However, since the parallel plate geometry does not shear the sample with a constant velocity across the plate surface, the fixture radius and gap height must be taken into account. Shear stress and shear rate for a parallel plate fixture are calculated using Equations 3.5 and 3.6, respectively, where shear rate is calculated for the radius at the edge of the fixture at gap height h.

$$\boldsymbol{\tau_{\theta Z}} = \frac{\boldsymbol{M}}{\boldsymbol{2\pi R^3}} \left[\boldsymbol{3} + \frac{\boldsymbol{d\ lnM}}{\boldsymbol{d\ ln\dot{\gamma}}}\right] \tag{3.5}$$

$$\boldsymbol{\dot{\gamma}_R} = \frac{\boldsymbol{R\Omega}}{\boldsymbol{h}} \tag{3.6}$$

Similarly, the length of the Mooney-Ewart Couette fixture must be taken into account when calculating shear stress. Equations 3.7 and 3.8 are used to calculate the shear stress and shear rate, respectively, for a Mooney-Ewart Couette geometry with a κ value (R_{inner}/R_{outer}) from 0.5-0.99.

$$\boldsymbol{\tau_{r\theta}(R_i)} = \frac{\boldsymbol{M_i}}{\boldsymbol{2\pi R_i^2 L}} \tag{3.7}$$

$$\boldsymbol{\dot{\gamma}(R_i)} = \frac{\boldsymbol{2\Omega_i}}{\boldsymbol{n\left(1-\kappa^{\frac{2}{n}}\right)}} \qquad \boldsymbol{where\ n} = \frac{\boldsymbol{d\ lnM_i}}{\boldsymbol{d\ ln\Omega_i}} \tag{3.8}$$

3.4.3 Thermogravimetric Analysis

Thermogravimetric analysis (TGA) is a characterization tool used to determine the degradation temperature of a material, or its components, in a controlled environment. In this research, a TA Instruments (New Castle, DE) TGA Q50 was used to determine the concentration of the aqueous CNC dispersions. A sample of 15 to 20 mg of CNC dispersion in a platinum pan was loaded in the TGA furnace and the initial weight of the dispersion was recorded. The furnace temperature was ramped at a rate of 10˚C/min until the furnace reached 120˚C. Air was fed to the furnace at a rate of 90 mL/min to the furnace throughout the run. The temperature was held constant for 30 minutes to ensure complete evaporation of the solvent. Finally, the weight of residual CNC was recorded and compared to the initial to generate a weight fraction.

3.5 Conductivity and Ionic Strength

Electrical conductivity measures a medium's ability to transport electric charge as a function of current density and electric field strength. Conductivity measurements were taken using a VWR International (Radnor, Pennsylvania) Traceable Expanded Range Conductivity Meter. Since ionic strength measures the concentrations of ions present in solution, conductivity can be related to ionic strength using Equations 3.9 and 3.10 [45].

$$\boldsymbol{Ionic\ Strength}\ [\boldsymbol{ppm}] = \boldsymbol{EC}\ \left[\frac{\mu \boldsymbol{S}}{\boldsymbol{cm}}\right] \times \mathbf{0.5} \tag{3.9}$$

$$\boldsymbol{Ionic\ Strength}\ [\boldsymbol{M}] = \frac{\boldsymbol{IS}\ [\boldsymbol{ppm}] \times \mathbf{10^{-3}}}{\boldsymbol{MW}\ [\frac{\boldsymbol{g}}{\boldsymbol{mol}}]} \tag{3.10}$$

Where EC is the electrical conductivity, IS is the ionic strength, and MW is the molecular weight of the solute. CNC dispersions used to measure conductivity were made

with refrigerated FPL stock gel (lot number 2016-FPL-CNC-098) and Millipore deionized water. Addition of sulfuric acid ended once the system achieved a conductivity of 1348 μS/cm. This conductivity value translates to an ionic strength equal to that of stable 12.1 wt% CNC gel; approximately 6.87×10^{-3} M of H_2SO_4. The chiral nematic pitch was measured from cross-polarized optical micrographs taken before and after H_2SO_4 was added to the CNC dispersion.

3.6 Fluid Phase Approach to Hydrolytically Stable CNC Films

A protocol to achieve hydrophobic films of CNC using fluid phase processing was adapted from Kim et al. [1]. The protocol began with the functionalization of cellulose with maleic acid groups through an esterification process depicted in Figure 15A. At 120˚C, the temperature at which esterification should occur at, sodium hypophosphite acts as a catalyst for the attachment of the maleic acid functional group. This was followed by a cross-linking reaction at 170˚C which used sodium hypophosphite as a cross-linking agent to bind maleic acid groups. This chemical reaction is depicted in Figure 15B.

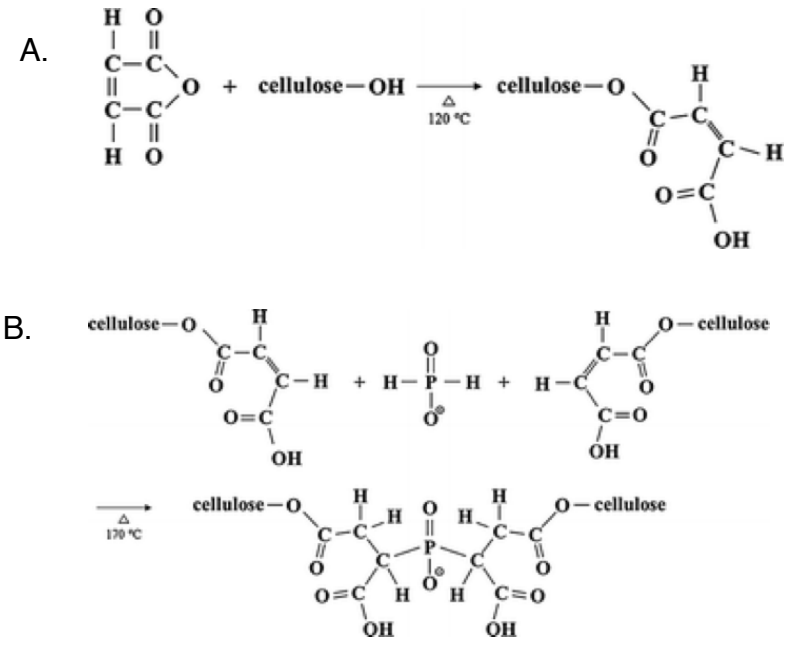

Figure 15 **A.** Functionalization of cellulose with maleic acid groups via esterification. **B.** Cross-linking of maleic acid groups present on adjacent cellulose molecules [1].

Maleic acid was added to aqueous CNC in a 10:1 ratio of maleic acid to anhydroglucose units present in the mixture followed by 5 wt% sodium hypophosphite. The slurry was mixed for 30 minutes at ambient temperature using a stir bar, then for an addition 30 minutes while being heated in a silicone oil bath at 120˚C. Unreacted

chemicals were removed by centrifugation at 3000 g for 10 minutes, after which the supernatant was removed from the solution. Remaining CNC at the bottom of the 30 mL centrifuge tube was redispersed in water and washed at 3000 g for an additional six cycles. The supernatant was discarded after each cycle and the CNC were vortex mixed to ensure homogeneity of the sample. To achieve fully crosslinked CNC/maleic acid films, thin films were cured at 170˚C in an oven immediately after they were sheared using a doctor blade coater.

3.7 Film Contact Angle

To characterize the hydrophobicity of CNC thin films, the water contact angles were recorded. Hydrolytic stability was qualitatively evaluated based on visual observation of films immersed in water. Contact angles are the equilibrium angle between the surface-liquid interface and the liquid-vapor interface, γ_{sl} and γ_{lv} using a given probe fluid [46]. In this case all contact angles were measured using deionized water at ambient temperature. For a drop of water to spread across a solid surface rather than sit idle in a finite space, the difference in interfacial energy between the solid-vapor and solid-liquid interface must be higher than the liquid-vapor interface. Rather, $\gamma_{sv} - \gamma_{sl} > \gamma_{lv}$ must be true for a drop of water to spread. The Young equation (Equation 3.11) describes the case in which equilibrium is reached so that the water droplet remains fixed in a finite area and appears below [46]. The Young equation is applicable for smooth surfaces; however, this equation can be altered so that it applies to roughened surfaces by multiplying the difference in interfacial energy by the roughened surface area, defined by σ.

$$\cos\theta = \frac{\gamma_{sv}-\gamma_{sl}}{\gamma_{lv}} \tag{3.11}$$

Water contact angle measurements were taken using a standard goniometer manufactured by ramé-hart instrument company (Succasunna, NJ). Figure 16 is a schematic of a droplet on the surface of an arbitrary substrate and measures the angle θ between the substrate and the liquid/vapor interface. Surfaces with a contact angle greater than 90˚ considered hydrophobic and those with a contact angle less than 90˚ are hydrophilic. Droplets were applied using an injection syringe with an approximate volume of 0.2 mL and angle measurements were captured using a charged coupled device, CCD, camera. Water contact angle measurements were taken at various locations of the CNC film to provide an initial determination for the uniformity of adsorbed, two-dimensional silane attached to the surface.

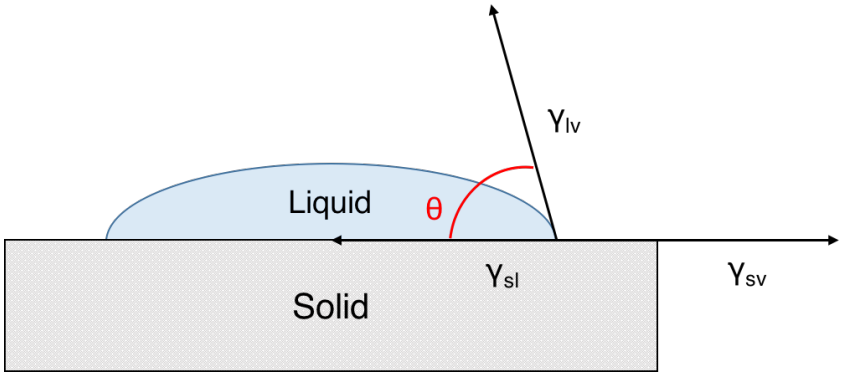

Figure 16 Schematic of a liquid droplet on the surface of a solid substrate [47].

3.8 CNC MEMS Fabrication

Fabrication of MEMS derived from thin film CNC followed a similar photolithographic approach used to fabricate any semiconducting device on a silicon substrate. The protocol used in this study was adapted from Ansari [2] and Haywood [40]. An initial anchor pattern was applied to a doped single crystalline silicon wafer using a

positive photoresist, AZ 5214 E-IR. A thin film of CNC was sheared on top of the anchor pattern and allowed to dry in the presence of a desiccant. A second coat of photoresist was applied onto of the surface of the CNC film and was used to expose the MEMS device layer. Multiple sensing devices were imprinted in chrome on the quartz device mask including mechanical stress testers, double clamped beams, and cantilever beam arrays which will be the target device highlighted in this research. Finally, a thin layer of TiO_2, approximately 10 nm, was applied to the surface of the substrate using electron beam deposition. Devices were etched in a plasma chamber with a coil power of 500 W and plate power of 300 W. Carbon tetrafluoride (CF_4) and oxygen were used to etch devices at a flow rate of 40 and 20 sccm, respectively. Etching cycles lasted for 30 seconds each and 16 to 18 cycles were needed to achieve defined MEMS devices. Once etched and imaged using a Nikon Eclipse 80i optical microscope equipped with an LU Plan Fluor 20X/0.50 NA objective lens, devices were diced into 1 cm squares and released. Diced samples were submerged in 99% isopropyl-alcohol and transferred to a critical point drier where carbon dioxide was used to remove residual photoresist. The critical point drier was operated at 1400 psi and 32˚C. Figure 17 shows an interferogram of a released cantilever beam array.

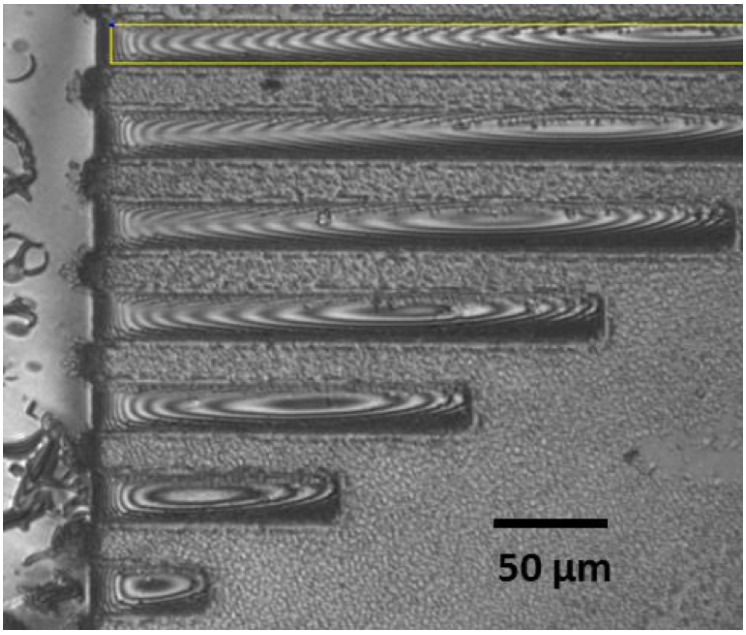

Figure 17 Interferogram of released microcantilever beams; Image taken by Partha Saha (Davis and Ashurst Group).

Chapter 4: Results

4.1 Rheology of CNC Dispersions

Rheology is an extremely sensitive method for understanding factors affecting the microstructure of dispersions. For example, Figure 18 shows factors that can influence CNC dispersion's steady shear viscosity by affecting the dispersion microstructure. When using rheology to understand microstructure it is important to understand the amount of experimental error and its sources. The instrument error for Anton Paar MCR301 steady shear viscosity measurements is 3 to 5% error based on Newtonian silicon oil rheology samples that are loaded on the instrument using best practices; the samples must be free of bubbles and a straight glassy edge between the plates or cone and plate must be visible. For complex fluids, additional sources of error can be due to dispersion inhomogeneity, inconsistent shear history between samples or tests, time dependent microstructural changes (e.g. settling, floc formation, aggregation), evaporation, changes in the gap edge, and slip at the fixture interface. For a given sample, each type of rheology fixture is prone to different types of errors [43]. Error resulting from shear history is typically negated by applying a pre-shear protocol that results in a consistent microstructure without causing shear induced alignment. Time dependent microstructural changes can be understood by performing a time series of amplitude sweeps within the viscoelastic region. In this fixed frequency oscillatory rheology test, the strain amplitude is increased to just below the limit of the linear viscoelastic region. Since this test should not result in any microstructural changes, any measured changes in rheological properties such as the storage modulus G' and loss modulus G" are due to time

dependent changes in the microstructure. Plotting data from successive amplitude weeps makes it easy to see when the changes exceed the tolerance for error (typically 10 – 20 %), and makes it possible to set the maximum time for measurement of each rheology sample. Evaporation changes result in changes in the amplitude sweep measurements and also result in the gap between plates (or cone and plate) becoming under-filled during testing. Any changes in the free surface at the gap affect the geometric assumptions for accurately measuring rheological parameters. In addition, evaporation can result in the microstructure gradients across the fixture radius. Skin formation or gelation at the free surface can result in higher apparent viscosities and storage moduli.

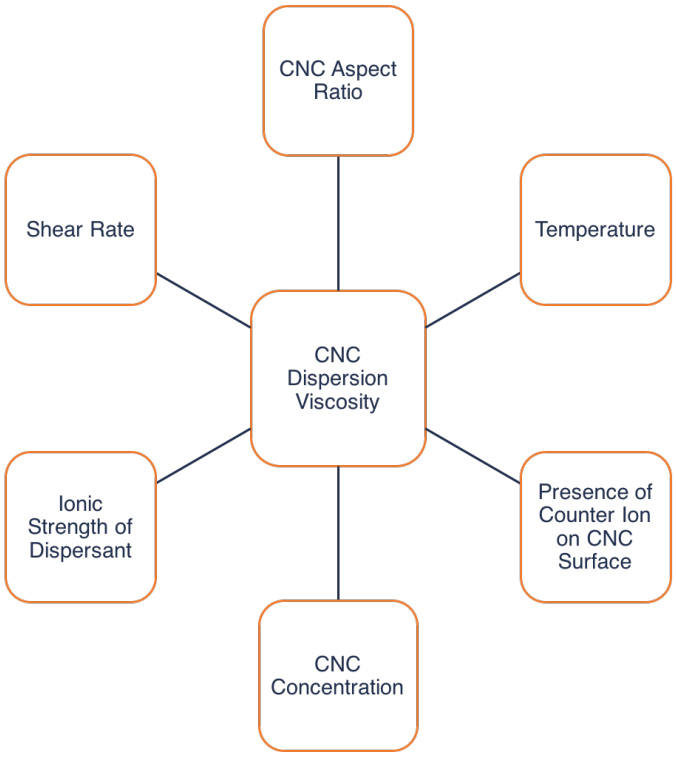

Figure 18 Factors influencing CNC dispersion viscosity measurements and microstructure.

4.1.1 Slip at Sample-Fixture Interface

Slip at the sample-fixture interface was a pervasive and often overlooked challenge at the start of this project. Viscosity measurements for a particular concentration, collected using various fixture gap heights, should be consistent across all sample loads since viscosity is a material property and independent of fixture gap. However, slip can be rheologically detected by a change in flow curve data based on fixture gap height. An example is shown in Figure 19, in which viscosity is plotted as a function of shear rate for an aqueous 4.48 vol% dispersion. Data was collected using a parallel plate fixture geometry with a 50 mm diameter at the following gap heights: 0.57, 0.92, and 0.97 mm. Viscosity measurement for this concentration had a wide range of reported values spanning from 0.91 Pa s to 3.6 Pa s for gap heights of 0.57 and 0.97 mm, respectively. This corresponds to a 74% difference in dispersion viscosity when there is less than half a millimeter difference in fixture gap height. This cannot be true as viscosity should remain constant at a particular shear rate. To cross-check parallel plate viscosity measurements, a 4.48 vol% sample was run using a Mooney-Ewart fixture which supported the measurements produced by the higher gap height. The large discrepancy between the two loadings at a gap of 0.97 mm are attributed to a combination of the sample not being completely homogenous and human error. To reduce variability in the data, a 15 minute pre-shear at a shear rate of 0.001 s^{-1} followed by a 10 minute relation period was implemented before step rate and flow curve data was collected. Viscosity measurements were also taken at consistent gap heights for each sample to mitigate discrepancies.

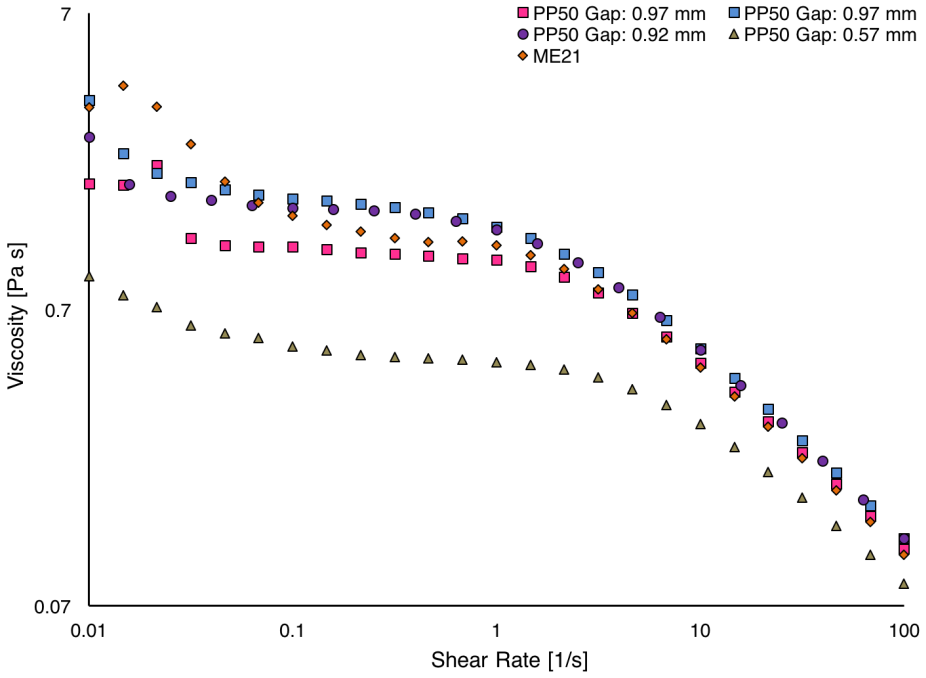

Figure 19 Plot of viscosity as a function of shear rate for a 4.48 vol% CNC dispersion at 25˚C.

4.1.2 Fixture Surface Finish

Surface finish has an effect on surface energy at a solid-liquid interface and can change the way a sample interacts with the surface it is in contact with [48]. A notable example of this is the hydrophobic surface of lotus leaves [49]. In general, differences in fixture roughness is not desirable when one is collecting rheological data. To determine the difference in surface roughness between the 25 mm and 50 mm diameter bottom plates, ellipsometry or atomic force microscopy could be used to determine subtle changes in plate fixtures. However, only water contact angle was measured to determine differences in wettability between the two surfaces. Water contact angle measurements were taken for both fixture diameters to see if surface roughness was the cause of discrepancies in reported viscosity. As expected, the 25 mm fixture had an average water

contact angle of 89.4˚, far greater than the 59.3˚ water contact angle measured for the 50 mm plate.

Differences in collected viscosity data for a 4.48 vol% dispersion, presented in Figure 20, were typically an order of magnitude apart where 25 mm fixture geometries resulted in higher viscosity measurements than 50 mm geometries. The cone and plate and parallel plate rheology data for the 25 mm fixtures was more consistent, but did not have the expected shape of the viscosity versus shear rate curves. Testing with the Mooney-Ewart Couette fixture supported viscosity measurements collected using 50 mm plate geometries. To control for this variability, all samples for the H_2SO_4 addition were run using 50 mm fixtures; unfortunately, the fixture dependent errors were not discovered before HCl tests were conducted. It should be noted that these discrepancies were unexpected and highly unusual. Although the fixtures have an obvious difference in surface finish they did not show any scratches or other damage. The fixtures give consistent data for a broad range of standard samples including silicon oils, polyethylene oxide solutions, and a lubricating grease. In previous research, checks for fixture related artifacts did not show any significant differences for a broad range samples including aqueous DNA, aqueous lysozyme, lab prepared aqueous CNC with H^+ counterions, silica nanorods in DMSO solutions, silver nanowires in ethylene glycol and water and carbon nanotube dispersions in thermoset resins, polymer solutions, and biomolecule solutions [50, 51, 22, 52, 53, 54, 55, 56, 57, 58].

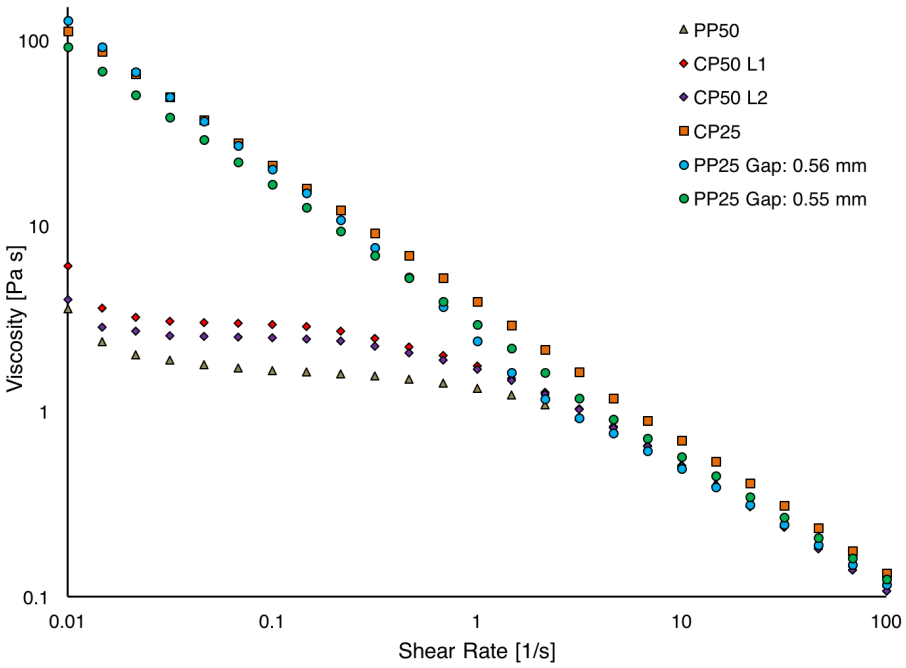

Figure 20 CNC Viscosity data comparing CP25 fixture to CP50 fixture for a 4.48 vol% dispersion.

4.1.3 Temperature Selection

Selection of the proper temperature to conduct rheological characterization was critical given that solvent evaporation over time can produce viscosity data that does not reflect the initial microstructure of the sample over the duration of a run. In the literature, there is not a consistently preferred temperature for characterizing CNC dispersions. In previous work in the Davis lab, Ureña-Benavides et al. performed the majority of characterization at 10˚C. They also explored the effect of temperature on viscosity [59, 22]. After running three different CNC dispersion concentrations (3.07, 6.99, and 12.1 vol%), the team found that isotropic dispersion viscosity decreased by 54% and biphasic dispersion viscosity decreased by 15% with increasing temperatures between 10˚C and 40˚C. This was attributed to changes in solvent viscosity temperature dependence of the phase boundaries and the fraction of liquid crystalline phase at each temperature [22].

However, due to strong network formation the 12.1 vol% liquid crystalline sample exhibited viscosity behavior that was independent of temperature between 10˚C and 35˚C but viscosity increased at 40˚C. However, the sample stability times at each temperature were not reported.

Oscillatory amplitude sweep tests were conducted on 6 and 9 wt% (3.83 and 5.81 vol%) samples to determine the amount of time a sample could run without solvent evaporation, or other changes, impacting its microstructure. Samples were pre-sheared for 5 minutes at a shear rate of 0.001 s^{-1} and allowed to relax for 15 minutes before starting the oscillatory shear test. The maximum strain was set to 2.15% and each sample was tested at a frequency of 10 s^{-1} at both 10 and 25˚C. Water was placed around the 50-mm parallel plate fixture to create a humid environment inside the evaporation hood which sealed the sample from ambient conditions. The results, shown in Figure 21, indicated that the 5.81 vol% sample experienced a 20% change in storage modulus (G') within 20 minutes. In contrast, the same CNC dispersion concentration saw a 14% change in 144 minutes of continuous oscillatory shear. The 3.83 vol% dispersion displayed a 34% change in G' in 37 minutes at 10˚C while at 25˚C, the sample dispersion saw a 19% reduction in 181 minutes. These unexpected results were confirmed by experiments run by another graduate student in the group. These results suggest that evaporation is more likely to occur at 10˚C which would negatively impact runs that last for over 2 hours. Although the reason behind this result is not entirely apparent, solvent evaporation could be due to the moisture content in the air surrounding the sample inside the evaporation hood. Condensation of water was present on the parallel plate fixture at 10˚C but not at

25˚C, which suggests that the air inside the evaporation hood was less humid at the lower temperature and could play a role in solvent evaporation at 10˚C. Therefore, all tests presented in this research were conducted at 25˚C to reduce artifacts due to evaporation.

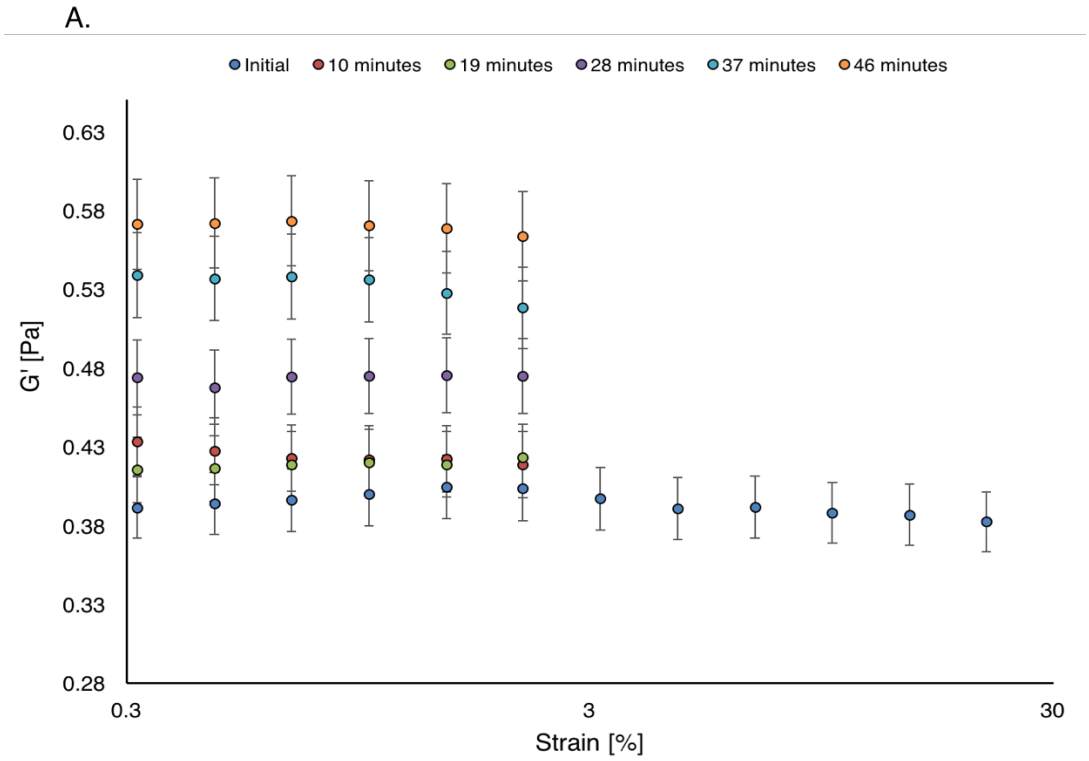

B.

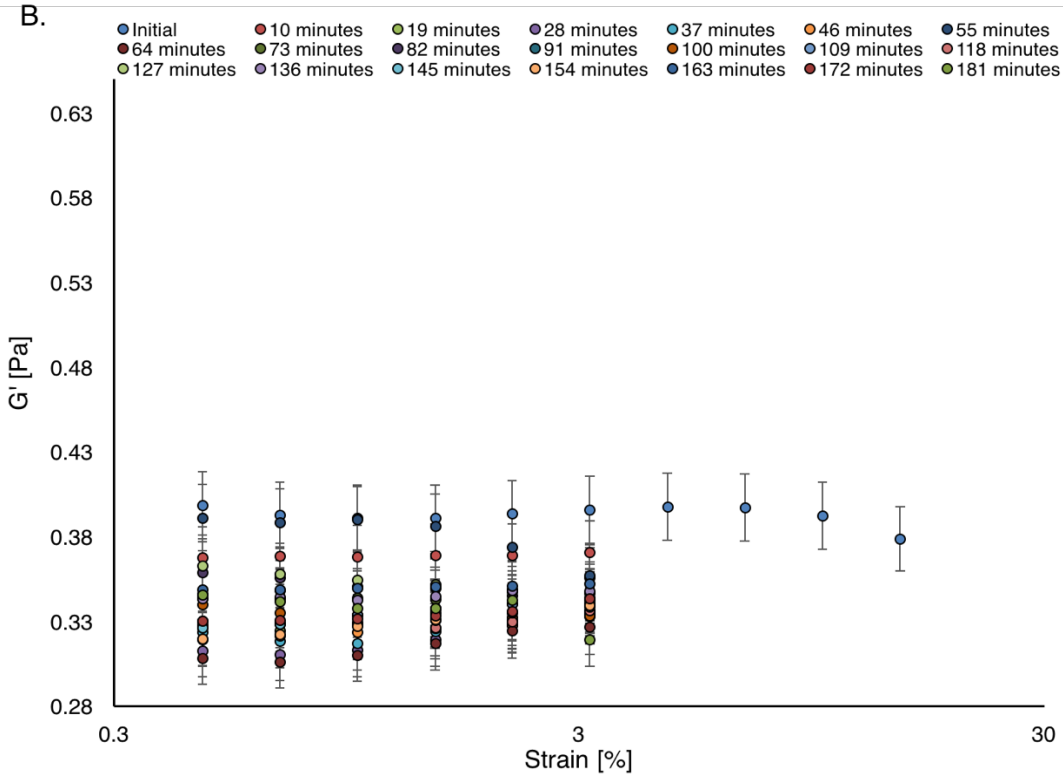
Initial
10 minutes
19 minutes
28 minutes
37 minutes
46 minutes
55 minutes
64 minutes
73 minutes
82 minutes
91 minutes
100 minutes
109 minutes
118 minutes
127 minutes
136 minutes
145 minutes
154 minutes
163 minutes
172 minutes
181 minutes
G' [Pa]
0.63
0.58
0.53
0.48
0.43
0.38
0.33
0.28
0.3
3
30
Strain [%]

C.

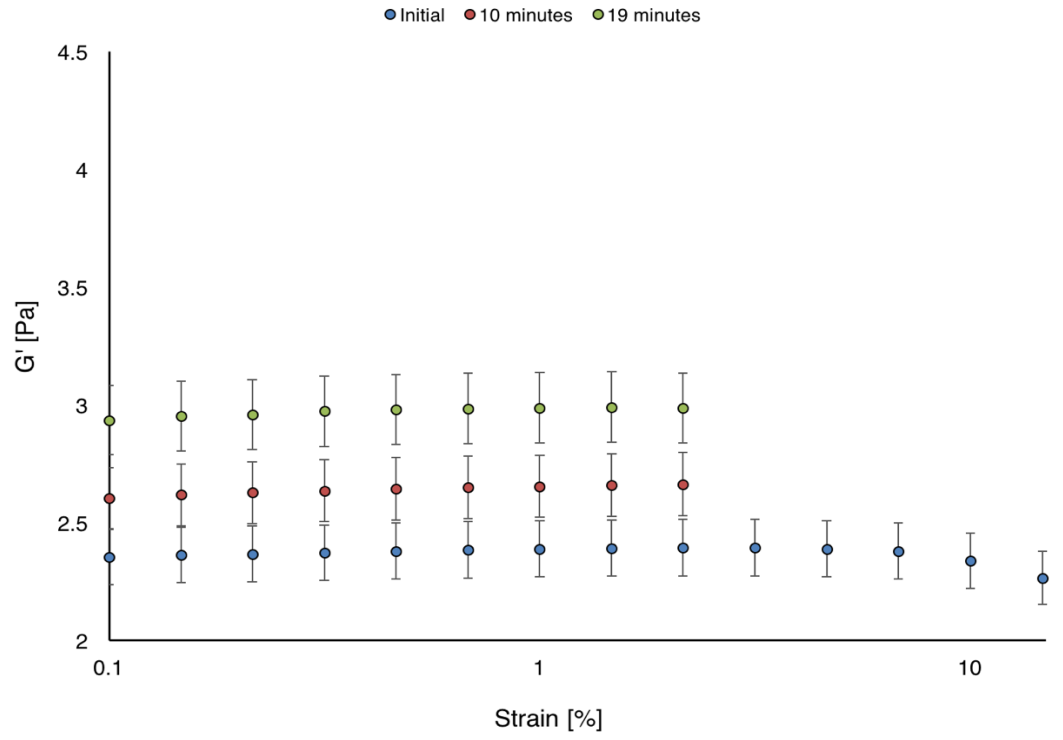
Initial
10 minutes
19 minutes
G' [Pa]
4.5
4
3.5
3
2.5
2
0.1
1
10
Strain [%]

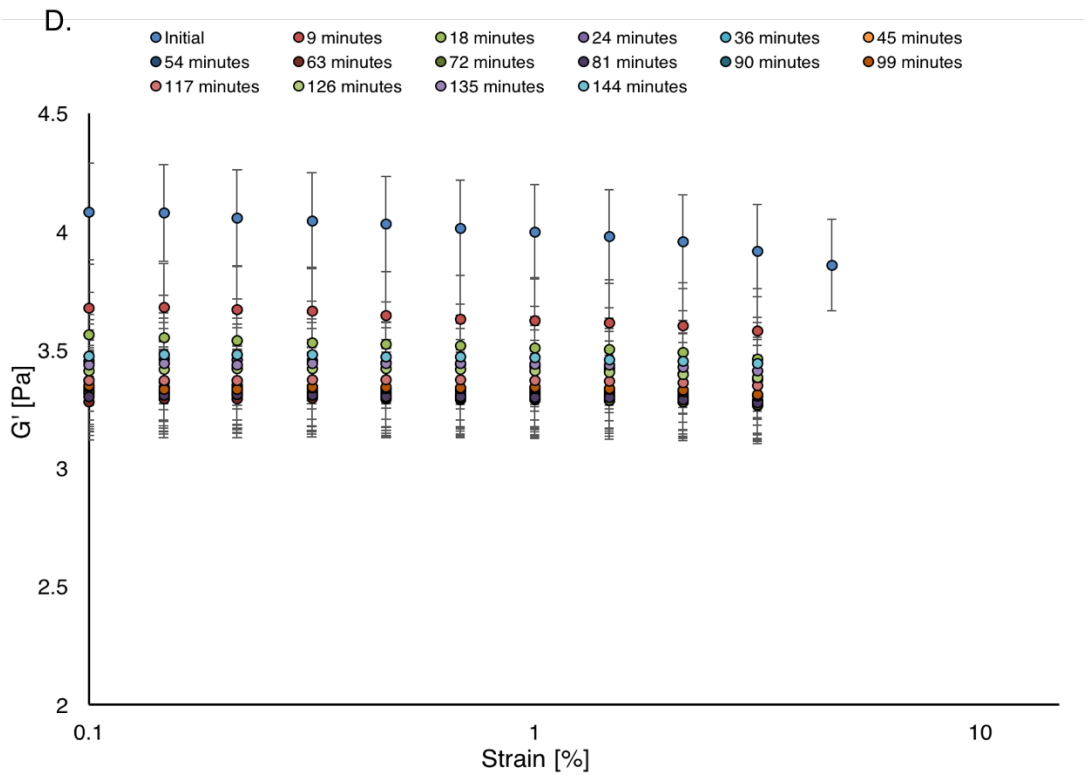

Figure 21 Continuous amplitude sweep plotted as a function of percent strain to test the effect of temperature on solvent evaporation. **A**. 3.83 vol% at 10˚C **B.** 3.83 vol% at 25˚C **C.** 5.81 vol% at 10˚C **D.** 5.81 vol% at 25˚C

4.2 Steady Shear Rheology of Cellulose Nanocrystal Dispersions

The following concentrations of CNC were used to rheologically characterize dispersion viscosity prior to the acid addition: 3.0, 5.0, 7.0, 9.0, 11.0, and 11.5 wt% (1.9, 3.2, 4.5, 5.8, 7.2, and 7.5 vol%). The CNC concentrations were chosen so that each of the phases was represented: isotropic (1.9 vol%), biphasic (3.2, 4.5, and 5.8 vol%), and liquid crystal (7.2 and 7.5 vol%). Each concentration was vortex mixed for 10 minutes and left overnight on a bottle roller to ensure uniform mixing before rheological measurements were taken. Figure 22 presents CNC dispersion viscosity as a function of shear rate for all concentrations. Shear thinning behavior, where viscosity decreases with increasing shear rate, is described by a power law model and is defined by Equation 4.1. In the equation, η is the apparent viscosity with units Pa s, K is the consistency coefficient, $\dot{\gamma}$ is the shear rate, and n is the power law index which is a variable parameter used to describe the fluid's behavior in response to shear. Multiple Power Law functions were used to fit shear thinning viscosity data across the tested shear rate range. This is expressed by multiple indices for a single concentration and was completed to highlight changes in CNC dispersion microstructure with increasing shear rate. Shear thinning fluids have an index less than 1, whereas shear thickening fluids, whose viscosity increases with shear rate, exhibit a power law index greater than 1. A similar technique was used in the literature to describe the shear thinning behavior of CNC dispersions [51].

$$\boldsymbol{\eta = K\dot{\gamma}^{n-1}} \tag{4.1}$$

From Figure 22, it is evident that high-end biphasic (5.8 vol%) and liquid crystal (7.2 and 7.5 vol%) dispersions exhibit a single power law shear thinning index across the entire shear rate range. This is similar to dispersions studied by Ureña-Benavides et al. (2011) and Shafiei-Sabet et al. (2014). [22, 59]. Viscosity data for 4.48 vol% and 3.18 vol% dispersions were fit to multiple power law equations based on shear thinning behavior at various inflection points in the empirical data. Power law indices and consistency coefficients used to fit empirical viscosity data can be found in Table 2. Shear rate ranges used to fit the power law equations were chosen based on inflection points in empirical viscosity data. Biphasic concentrations (3.18 and 4.48 vol%) follow the three-region viscosity profile, outlined by Onogi and Asada for liquid crystal regime samples, mentioned in Section 2.2.3. This same profile was seen in the literature for biphasic CNC dispersions and not for liquid crystal concentrations [60, 13] by by Ureña-Benavides et al. (2011) and Haywood et al. (2017) [22, 51]. This flow behavior does not hold true for the isotropic dispersion (1.89 vol%) as the dispersed rods at this concentration require a higher shear rate for flow alignment and exhibit a Newtonian plateau across the investigated shear rate range. Viscosity plotted as a function of dispersion concentration at three different shear rates is presented in Figure 23. From this, it is evident that CNC viscosity continuously increases with increasing dispersion concentration; congruent with findings reported in the literature [22].

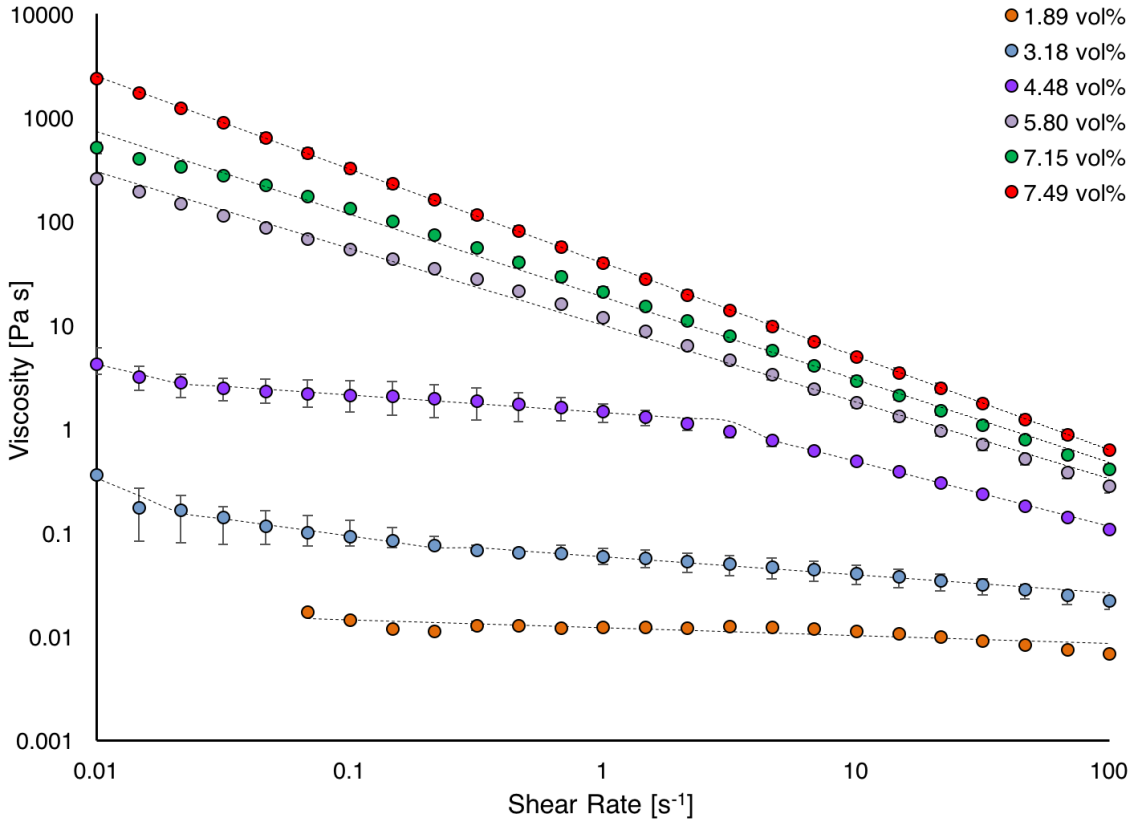

Figure 22 Viscosity as a function of shear rate for isotropic [1.89 vol% (orange)], biphasic [3.18 vol% (blue), 4.48 vol% (dark purple), 5.80 vol% (light purple)], and liquid crystalline [7.15 vol% (green), 7.49 vol% (red)] CNC dispersions.

Table 2 Power law indices used to fit viscosity data prior to acid addition with corresponding shear rate ranges.

Concentration (vol%)	Shear Rate (s^{-1})	PL Index (n)	Consistency Coefficient (kg/m)
7.49	0.01 – 100	0.01	39.82
7.15	0.01 – 100	0.20	18.70
5.80	0.01 – 100	0.26	9.98
4.48	0.01 – 0.02 0.03 – 3.16 4.64 – 100	0.44 0.83 0.38	0.32 1.44 2.04
3.18	0.01 – 0.02 0.03 – 0.22 0.32 – 100	0 0.67 0.83	3.35×10^{-3} 4.34×10^{-2} 5.88×10^{-2}
1.89	0.01 – 100	0.92	1.22×10^{-2}

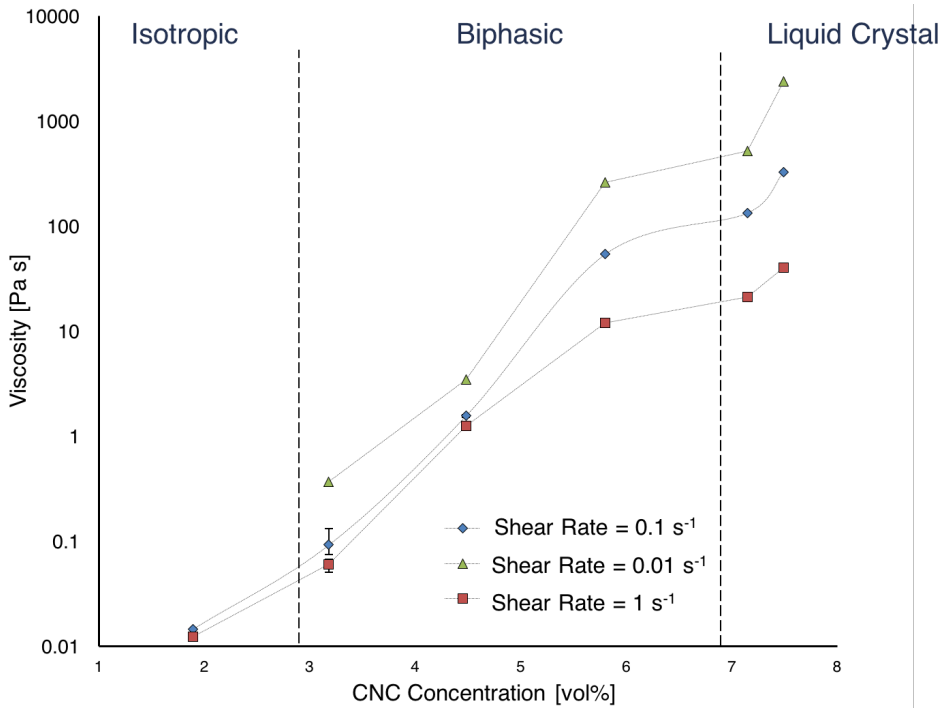

Figure 23 FPL-CNC viscosity as a function of dispersion concentration at 0.01, 0.1, and 1 s^{-1}. Error bars indicate maximum and minimum viscosity values. Lines connecting viscosity measurements are used to guide the eye and to not indicate a trend present in the collected data.

4.3 Cross Polarized Microscopy & Pitch Measurements

Chiral nematic pitch length was measured for each concentration of CNC dispersion and a plot of average pitch length as a function of CNC dispersion concentration is displayed in Figure 24. When viewed under a cross-polarized light microscope, biphasic dispersion concentrations exhibit birefringent domains which appear as a distinct fingerprint texture. As previously stated, pitch length correlates to the distance spanning two white lines and two black lines of the fingerprint texture seen in microscopy images. At each concentration, pitch length is accompanied by a cross-polarized microscope image depicting the sample used to measure 25 pitch lengths at various points on the sample. Data was averaged and the standard deviation was

calculated to produce error bars on each average pitch length. With increasing concentration of CNC, there was a notable decrease in chiral nematic pitch length; from 8.9 μm at 2.85 vol% to 5.1 μm at 5.14 vol%. The possible local minimum at 4.48 vol% could indicate a phase transition from a biphasic to the liquid crystalline regime. However, since isotropic regions were still present at 4.81 and 5.14 vol%, it is evident that 4.48 vol% still lies within the biphasic phase regime. One would need to compare microscopy and pitch measurements to the steady shear flow curve behavior to conclusively determine this finding. If the flow curve exhibited Region II and an elongated Region III behavior, regarding Onogi and Asada's three region viscosity flow curve seen in Figure 7, then this correlation would most likely indicate a phase transition near ϕ_{LC} concentration. However, the viscosity versus shear rate curve for 4.48 vol% CNC exhibits all three regions and therefore, one can glean that ϕ_{LC} lies at a higher concentration than 4.48 vol%.

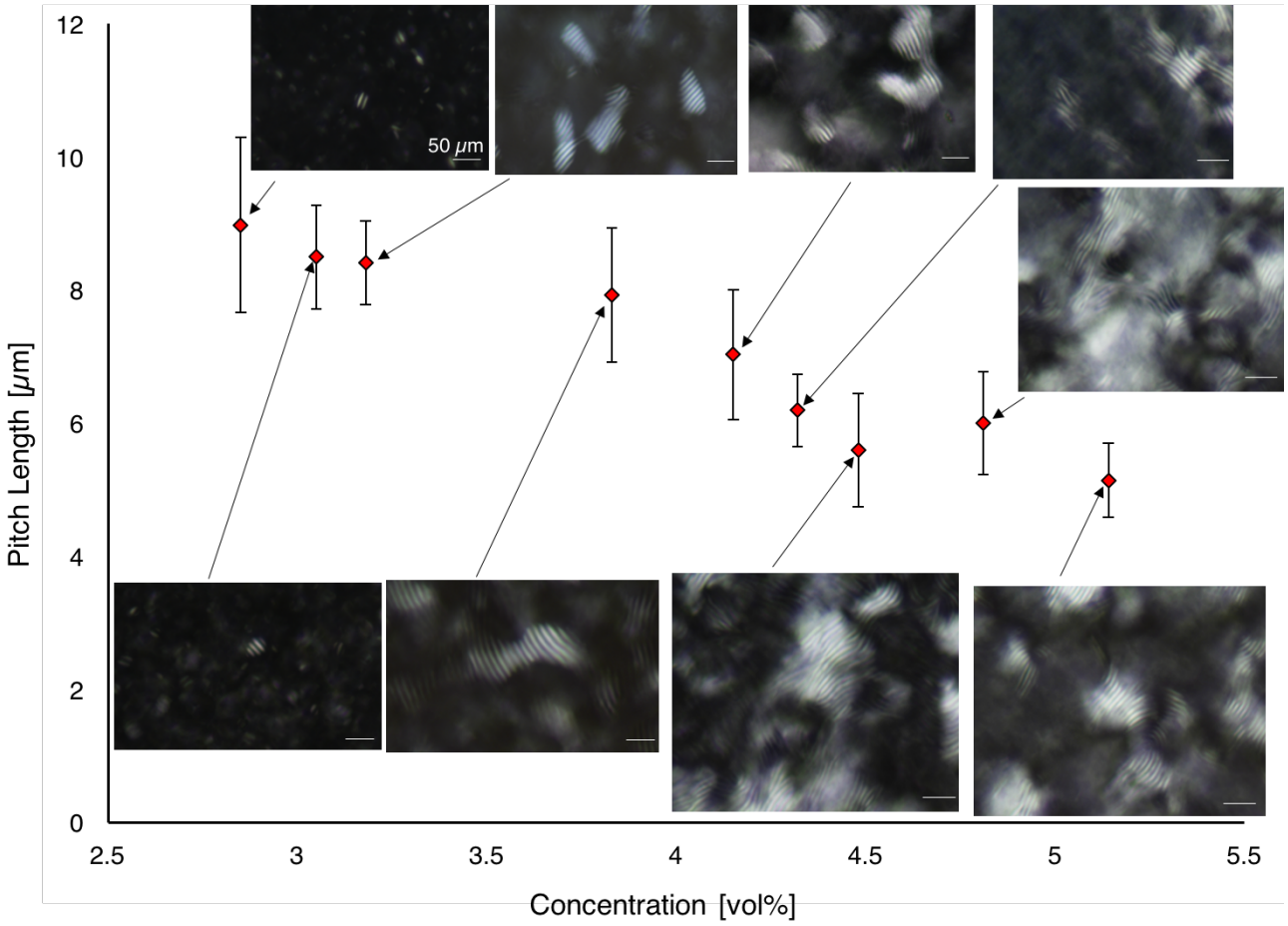

Figure 24 Pitch length as a function of CNC concentration for aqueous cellulose nanocrystal dispersion. All sale bars represent a length of 50 μm.

4.4 Hydrochloric Acid Addition to Cellulose Nanocrystal Dispersions

To study the effect of holding ionic strength constant across a range of CNC dispersion concentrations, 0.01 M aqueous hydrochloric acid (HCl) was added to achieve a target pH value of 5.86. This protocol was adapted from Dong et al. in which the team studied the effect of electrolyte concentration, and subsequently ionic strength, on aqueous CNC dispersions through the addition of HCl, sodium chloride (NaCl), and potassium chloride (KCl). [28] The approach used in this study differed from that of Dong et al. in that this experiment held ionic strength constant across dispersions of various

CNC dispersion concentration whereas Dong held CNC concentration constant to characterize the effect of added electrolyte. Additionally, Dong et al. analyzed the effect of added electrolyte had on isotropic and anisotropic volume fraction rather dispersion viscosity. Since ion concentration increases with CNC concentration, it is easier to see the effect of ions on dispersion microstructure if total ion concentration is held constant. This was accomplished by monitoring dispersion pH during the acid addition, approximately 200-1400 μL of 0.01 M HCl depending on CNC concentration. All tests on dispersions with added hydrochloric acid were completed using 20 mL samples of FPL-CNC lot number 2015-FPL-CNC-077.

Hydrochloric acid was chosen to be the added electrolyte for its complete dissociation in an aqueous environment and, at the time, hydrogen was thought to be the cation present near the nanorod surface. Later, it was found out that the CNC sourced from the USDA FPL had a sodium, rather than hydrogen, as the counterion [5]. A target pH value of 5.86 was chosen to be the stop point for HCl addition because this was the value measured for a 7.15 vol% CNC gel, the nanocrystal concentration of the stock gel received from FPL. At this concentration and pH value, the liquid crystal dispersion appeared stable and therefore, it was hypothesized that dispersions with a lower cellulose content would also remain stable at this pH value.

When dispersion concentration is held constant, the addition of aqueous hydrochloric acid results in a decrease in dispersion viscosity. Cross-polarized optical micrographs were taken of each dispersion concentration and were subsequently used

to measure chiral nematic pitch after the addition of HCl. Figure 25 plots pitch measurements before and after acid addition as a function of dispersion concentration.

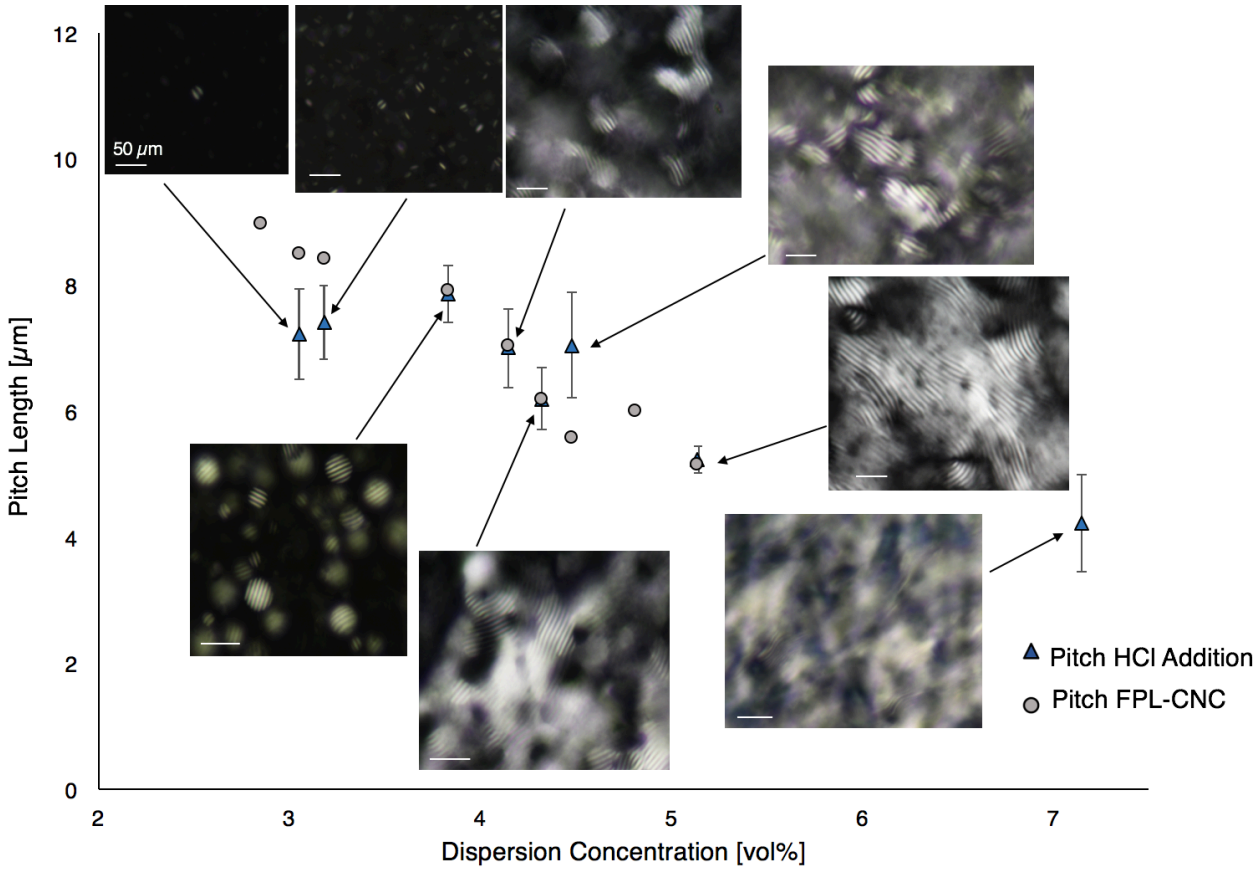

Figure 25: Plot of average pitch length as a function of dispersion concentration post-HCl addition. Error bars indicate standard deviation in pitch for 25 measurements and all scale bars at 50 μm in length.

At low concentrations, $\phi \leq 3.18$ vol%, average pitch length decreased by at least 1 μm, which indicates an increase in rod-rod interactions because of the addition ions present in the dispersion [61]. For dispersions with a CNC concentration of 3.83 and 4.15 vol%, no statistical change in average pitch length was recorded after the addition of hydrochloric acid. This could be the result of the low acid concentration, 0.01 M, added to these dispersions and more tests should be conducted to determine if this finding reflects the exact pitch behavior. However, at 4.48 vol% CNC, average pitch length

increased by approximately 1.4 μm after the addition of HCl. Although the reason behind this increase in pitch length is unclear, as this phenomenon is not mentioned in the literature, one can hypothesize that repulsion between dispersed charged rods minimizes entropy in the system and results in an increased pitch length. At higher CNC concentrations, average pitch length decreased for both sets of measurements. The datasets overlapped at 5.14 vol% and no statistical difference in average pitch length was recorded. However, additional measurements need to be taken at this concentration.

Steady shear rheology was performed on eleven different CNC dispersion concentrations at shear rates ranging from 0.01 to 100 s^{-1} using the following fixture geometries: 50 mm and 25 mm parallel plate, 50 mm and 25 mm cone and plate, and a Mooney-Ewart couette fixture (ME21). Rheometry on low viscosity dispersions were run using fixtures with the greatest surface area, e.g. ME21 and CP50, to achieve a minimum torque measurement of 0.1 μNm at as low as possible a shear rate. Viscosity data taken at a shear rate of 0.01 s^{-1} post-HCl addition is plotted as a function of dispersion concentration in Figure 26. The break in the y-axis indicates that the viscosity of 7.15 vol% was three orders of magnitude larger than the other reported viscosity measurements and no viscosity measurements were taken at intermediate dispersion concentrations. Despite holding pH constant for all dispersions, no relative maximum was recovered for aqueous CNC. Furthermore, viscosity data plotted at higher shear rates exhibits the same general trend and is presented in Figure 27, albeit shifted downward as a shear rate increase.

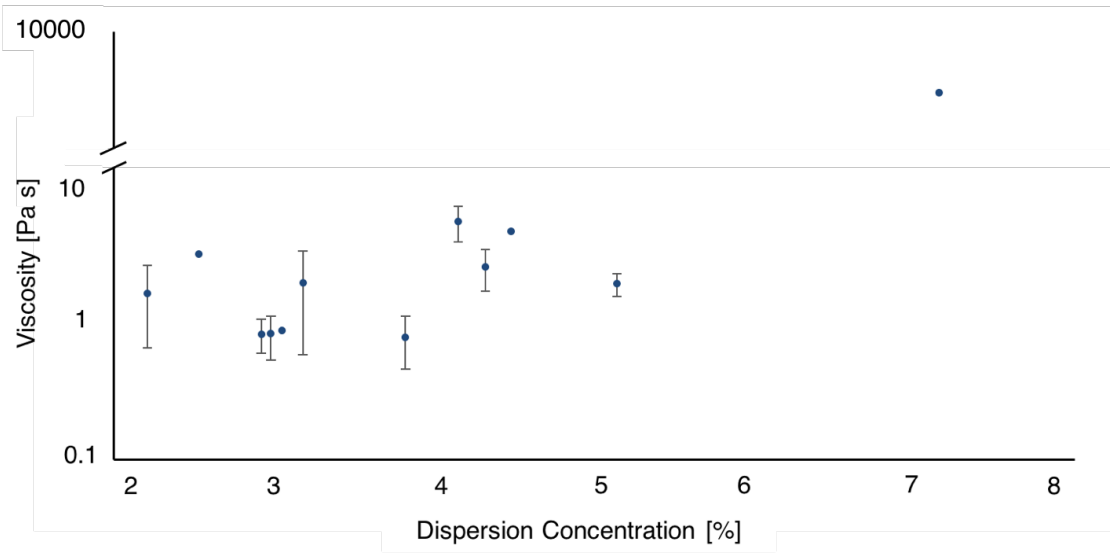

Figure 26 CNC viscosity as a function of dispersion concentration post-hydrochloric acid addition at 0.01 s^{-1} shear rate and 25˚C.

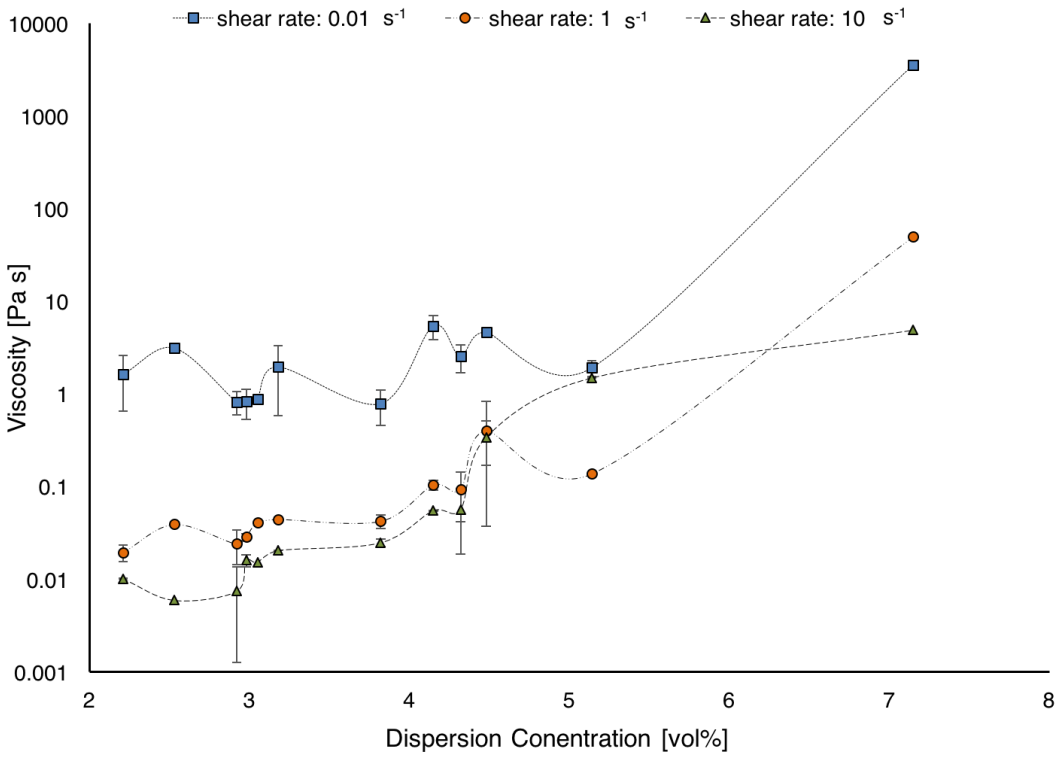

Figure 27 Flow curve of aqueous CNC dispersions at three different shear rates: 0.01, 1, and 10 s^{-1}. Lines connecting viscosity measurements are used to guide the eye and to indicated a trend present in the collected data.

From this work, it is evident that ions present in solution have a non-negligible impact on the microstructure of CNC dispersion. Viscosity measurements for biphasic dispersions of CNC tend to have greater variability than both isotropic and liquid crystal dispersions, particularly when an electrolyte is added to the system to increase its ionic strength. As such, it is difficult to identify the critical concentration ϕ_{LC} from the limited number of concentrations presented above. However, based on cross-polarized optical microscopy and the appearance of a single anisotropic birefringent domain, one can conclude that critical concentration ϕ_i after the addition of 0.01 M HCl lies at 3.05 vol%. Accurate determination of phase transition concentrations cannot rely on rheological analysis alone, one must combine this with cross-polarized optical microscopy. A local maximum in the biphasic region followed by a local minimum at ϕ_{LC} was not recovered for aqueous CNC dispersions despite the addition of hydrochloric acid. This could come as a result of the low concentration or small volume of HCl added to each CNC dispersion. As a result, the added electrolyte was changed from 0.01 M HCl to 0.1 M H_2SO_4 and ionic strength was measured using conductivity rather than pH.

4.5 Sulfuric Acid Addition to Cellulose Nanocrystal Dispersion

After FPL dialyzes the CNC slurry to remove impurities, CNC is known to retain some sodium cations which in turn keeps the suspension stable over more considerable period [10]. Dissociated sodium cations and chlorine anions in dispersion had the potential to crash out of suspension which would impact rheological measurements taken

on the sample. To mitigate this risk, 0.1 M aqueous sulfuric acid (H_2SO_4) was substituted as the added electrolyte.

Sulfuric acid (64 wt%) was purchased from Sigma Aldrich and diluted to a 0.1 M aqueous solution. H_2SO_4 was added incrementally to 20 mL of dispersions with the following concentrations of CNC: 7.15, 5.81, 4.48, 3.18, and 1.89 vol%. Dispersions were vortex mixed for 5 minutes after each addition of aqueous H_2SO_4 and conductivity readings were recorded immediately using a VWR Traceable Expanded Range Conductivity meter. CNC pitch length is plotted as a function of dispersion concentration in Figure 28. Similar to that of CNC data without the addition of acid, average pitch length decreased with increasing CNC concentration (and dispersions viscosity)

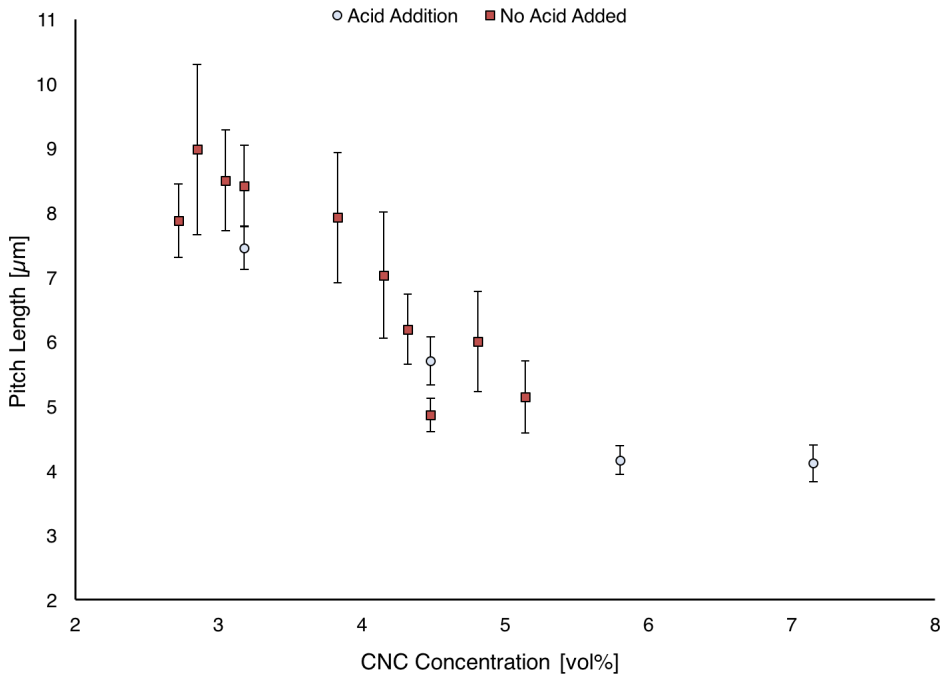

Figure 28 Average pitch length before sulfuric acid addition [red squares] is compared to pitch length after acid addition [black diamonds] as a function of concentration. Error bars indicate standard deviation of 25 pitch measurments.

Steady shear viscosity measurements were taken for each concentration using the following fixture geometries: 50 mm parallel plate, 50 mm cone and plate, and a 21 mm Mooney-Ewart. Geometries were chosen based on their ability to meet the 0.1 μNm torque minimum at as low as possible a shear rate. Figure 29 illustrates dispersion viscosity as a function of shear rate for each concentration tested, ranging from 1.89 to 7.15 vol%. Viscosity values are averaged between four sample loads on two different fixture geometries. Error bars signify minimum and maximum viscosity measurements at a particular shear rate. Power law index values are presented for each dispersion concentration in Table 3. Multiple indices are listed for a single concentration for cases where multiple power law equations were used to closely model empirical data. Shear rate ranges used to fit power law model were chosen based on inflection points in empirical viscosity data.

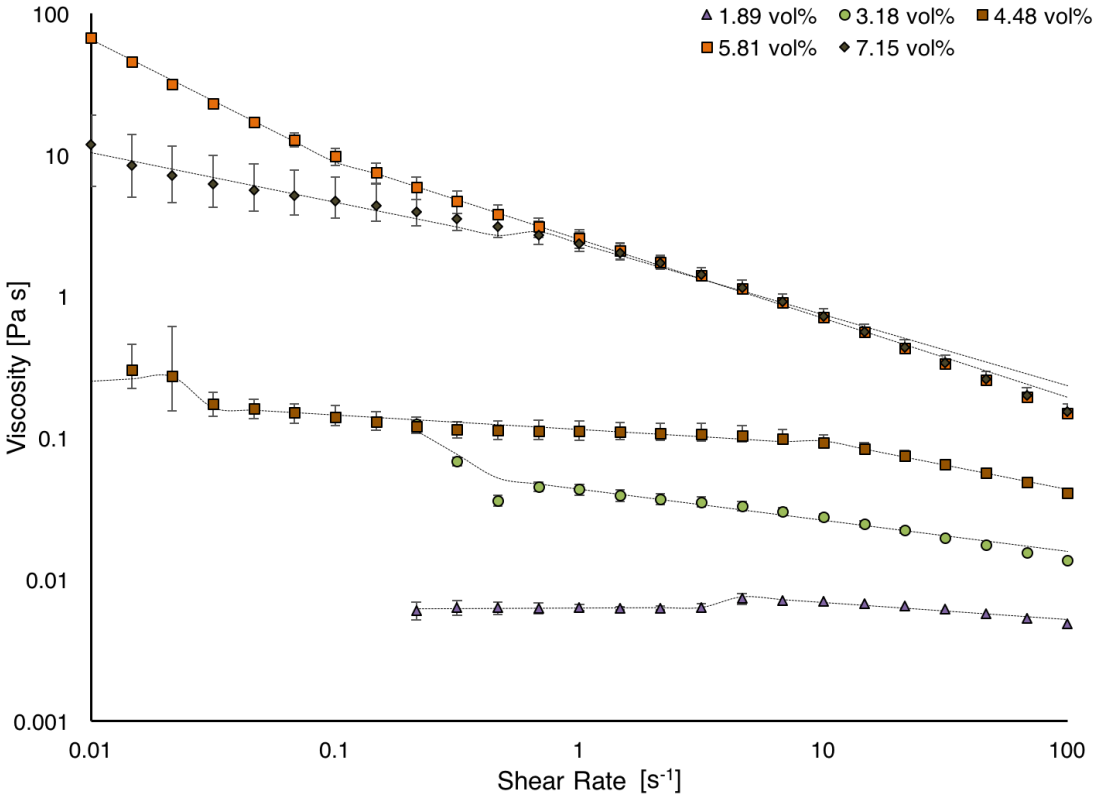

Figure 29 Viscosity as a function of shear rate after sulfuric acid addition. Data is fit to a Power Law Model, which is indicated by dashed lines.

Table 3 Power law indices used to fit viscosity data post H_2SO_4 addition with corresponding shear rate ranges.

Concentration (vol%)	Shear Rate (s^{-1})	PL Index (n)	Consistency Coefficient (kg/m)
7.15	0.01 – 0.46 0.68 – 100	0.65 0.50	2.07 2.37
5.81	0.01 – 0.1 0.15 – 100	0.14 0.44	1.22 2.54
4.48	0.01 – 0.02 0.03 – 6.81 10 – 100	1.10 0.90 0.66	0.40 0.11 0.21
3.18	0.22 – 0.46 0.68 – 100	0 0.78	2.43×10^{-2} 4.36×10^{-2}
1.89	0.22 – 3.16 4.64 – 100	1.01 0.88	6.30×10^{-3} 9.19×10^{-3}

Figure 30 presents viscosity data as a function of dispersion concentration at 0.01, 0.2115, and 1 s^{-1} shear rates. The plot indicates that CNC viscosity continuously increases with dispersions concentration at moderate and high shear rates, even in the presence of excess sulfuric acid. This trend was not seen for concentrations at 0.01 s^{-1} where the viscosity of the 5.81 vol% dispersion was greater than that of the 7.15 vol% dispersion. However, more data needs to be collected at low shear rates to confirm if this is indicative of a relative maximum in the viscosity versus concentration curve.

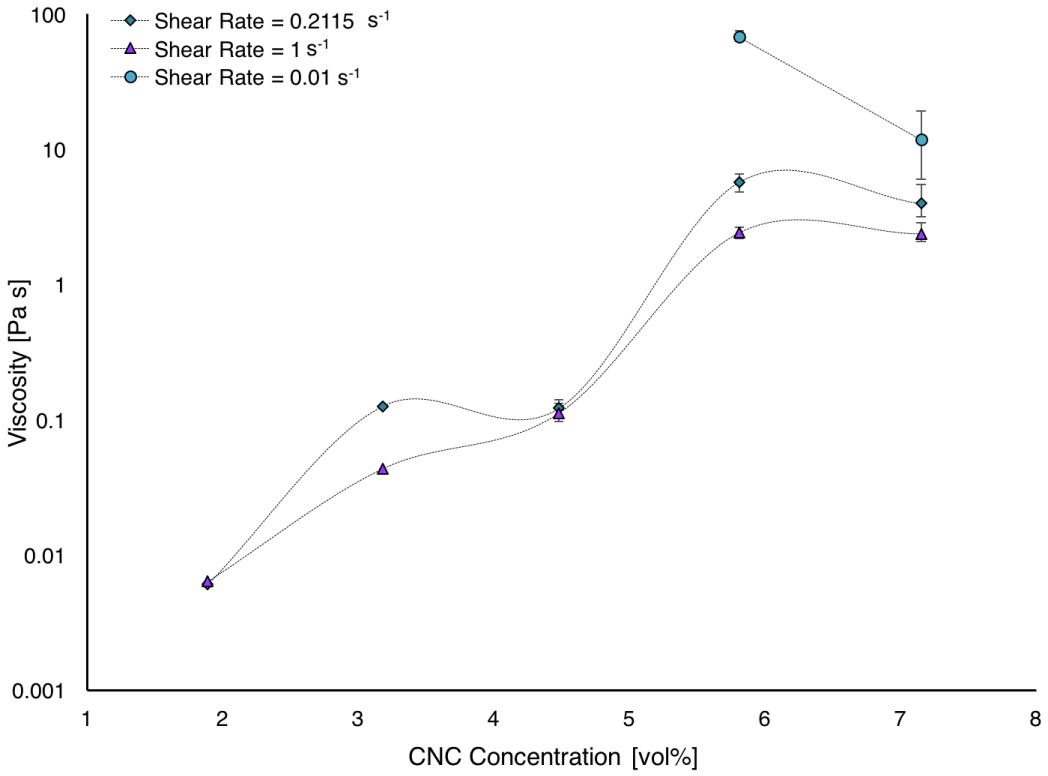

Figure 30 Viscosity as a function of CNC dispersion concentration at three shear rates: 0.01, 0.2115, and 1 s^{-1}. Lines connecting viscosity measurements are used to guide the eye and not to indicate a trend present in the collected data.

One noteworthy finding differentiates data collected before and after H_2SO_4 was added to FPL-CNC dispersions. With regard to Figure 29, low shear viscosity data for

5.81 vol% is nearly an order of magnitude higher than that of 7.15 vol%. One can assume that the addition of H_2SO_4 significantly weakens the liquid crystalline structure of FPL-CNC dispersions, most likely due to an increase in electric double layer thickness among dispersed rods. Shafiei-Sabet et al. found this same phenomenon for gel samples with CNC concentrations greater than 11 wt% and an ionic strength less than 10 mM NaCl. [60] For salt concentrations 10 mM or higher, they found that viscosity increased for concentrations that cross the gel threshold and attributed this increase in viscosity to CNC aggregation.

Steady shear viscosity data suggests that sulfuric acid addition had the most significant effect on the 7.15 vol% CNC dispersion; which exhibited a decrease in viscosity from 516 to 11.8 Pa s. Figure 31 displays a plot of dispersion viscosity as a function of shear rate for 7.15 vol% before and after H_2SO_4 addition. Cross-polarized optical micrographs highlight the phase shift resulting from the addition of H_2SO_4.

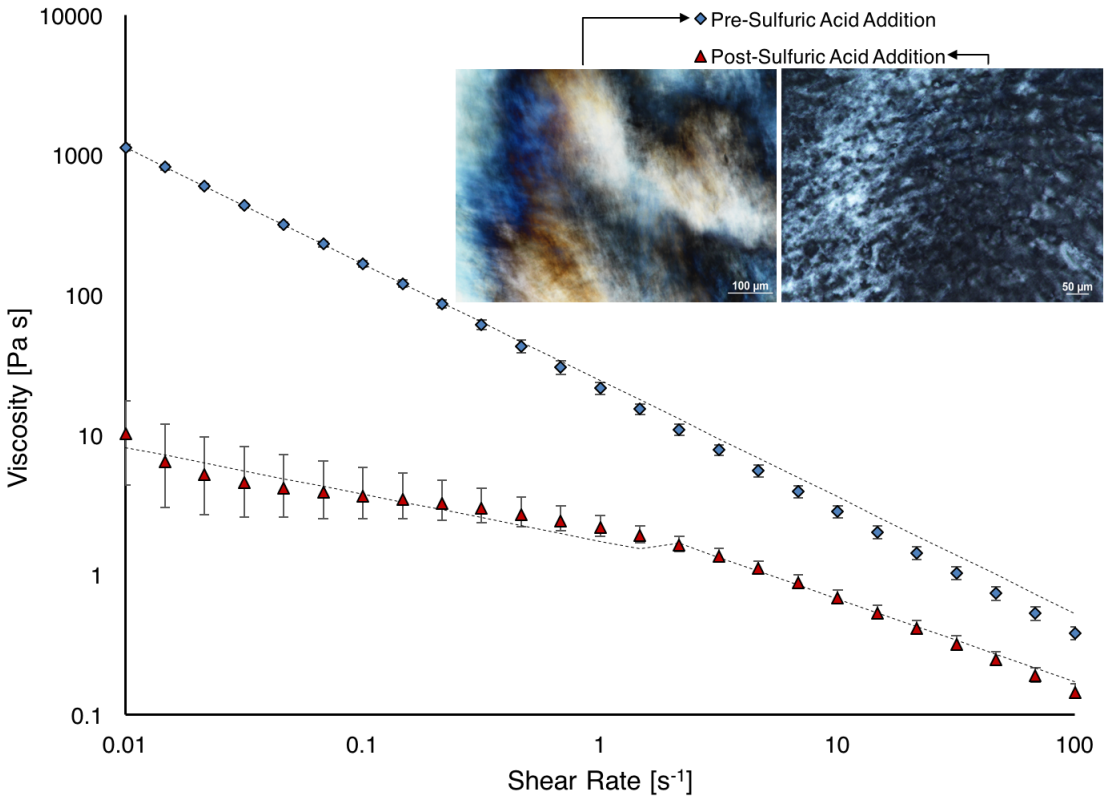

Figure 31 Flow curve for 7.15 vol% dispersion, before and after sulfuric acid addition, accompanied by cross-polarized optical micrographs depicting each sample tested. Error bars indicate minimum and maximum viscosity measurements. Dashed line indicates power law viscosity prediction.

Shafiei-Sabet et al. also analyzed shear rheological data for biphasic CNC concentrations while varying ion concentration. They found that low shear viscosity increases with increasing ion concentration yet high shear viscosity decreases with increasing ion concentration [60]. They attribute this shift in viscosity to the arrangement of anisotropic domains present in the biphasic dispersions. Specifically, the increase in dispersion viscosity at low shear rates is indicative of higher chiral nematic interaction between nanocrystals present which is further supported by a decrease in pitch length. At high shear rates, individual nanocrystals present align in the direction of flow, resulting in a decreased dispersion viscosity [60]. This characterization of biphasic CNC dispersion

holds true for 3.18 vol% samples tested in this study. Figure 32 depicts this change in dispersion viscosity as a function of the shear rate before and after H_2SO_4 addition. Consistent with the study performed by Shafiei-Sabet et al., a decrease in average pitch length was reported for the 3.18 vol% dispersion with excess H_2SO_4 from 8.42 to 7.45 μm

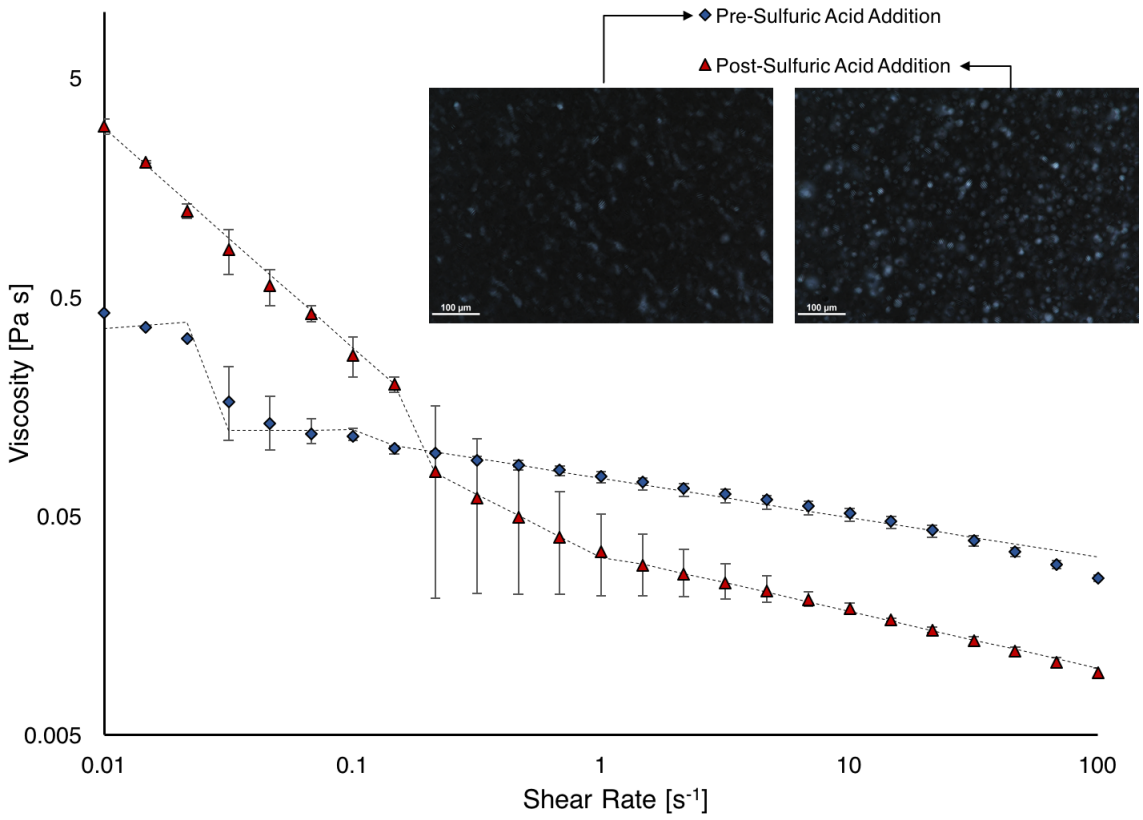

Figure 32 Viscosity as a function of shear rate for 3.18 vol% dispersions before and after sulfuric acid addition. Error bars indicate minimum and maximum viscosity measurements.

Given the established parallels between viscosity measurements reported in this study and those of Shafiei-Sabet et al. for biphasic dispersions, one would assume that samples of 4.48 vol% CNC with added electrolyte follow the same trend. However, Figure 33 suggests that 4.48 vol% behaves similarly to an entirely liquid crystalline dispersion in that viscosity is reduced upon H_2SO_4 addition across all shear rates. There also appears to be an elongation in the Newtonian plateau at intermediate shear rates; this plateau is

typically indicative of wagging among dispersed rods. If continued, future work should include more viscosity data collection for biphasic CNC dispersions to elucidate the critical concentration when viscosity versus shear rate behavior begins to resemble 4.48 vol%. Analysis of cross-polarized optical micrographs suggests that there is a noticeable increase in average pitch length for the 4.48 vol% dispersion; from 4.9 μm seen in standard CNC to 5.7 μm seen in dispersions with excess H_2SO_4. This increase in average pitch length is indicative of decreased nanocrystal interaction and subsequently decreased viscosity.

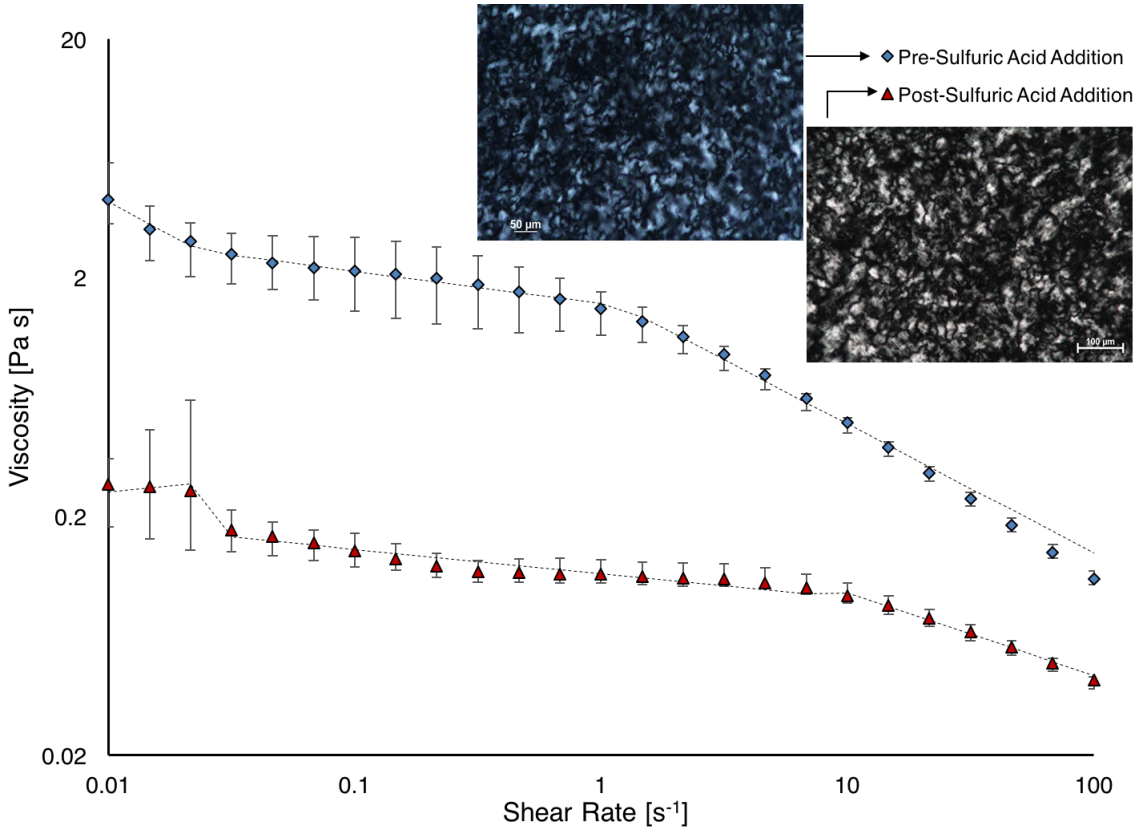

Figure 33 Viscosity as a function of shear rate for 4.48 vol% CNC dispersion before and after sulfuric acid addition. Error bars indicate the minimum and maximum viscosity measurements.

A decrease in dispersion viscosity upon the addition of H_2SO_4 is also exhibited by 5.81 vol% dispersion samples. From the cross polarized optical microscopy depicted in Figure 34 a noticeable shift in dispersion phase behavior from that of a liquid crystalline regime to a biphasic regime occurred when ionic strength increased. This further supports the previous notion that the electric double layer surrounding CNC is expanded and weakens nanocrystal interaction. More samples should be analyzed to confirm this rationale as this decrease in viscosity could also be attributed to a difference in CNC aspect ratio between CNC used in each study and, to a lesser extent, the presence of Na^+ ions present in this dispersion.

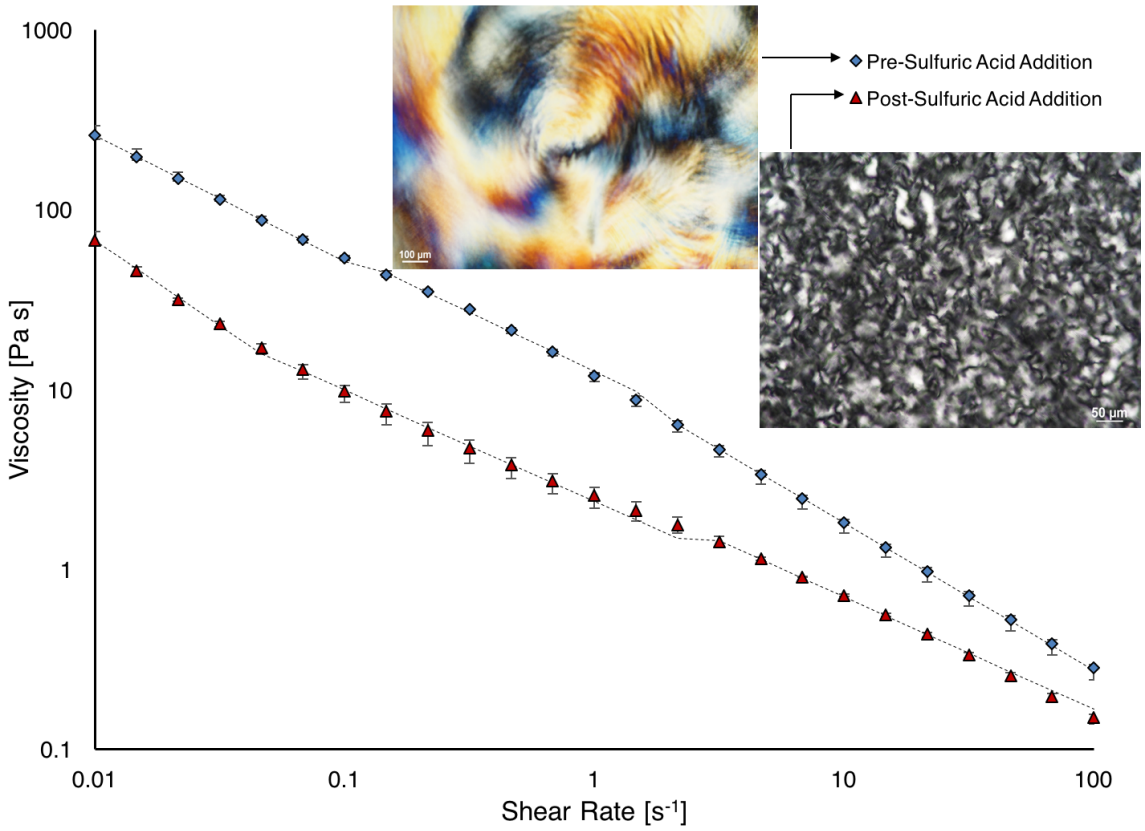

Figure 34 Viscosity plotted as a function of shear rate for 5.81 vol% CNC dispersion before and after sulfuric acid addition. Error bars indicate the minimum and maximum viscosity measurements.

Finally, isotropic samples from a 1.89 vol% dispersion were probed to determine the impact excess aqueous sulfuric acid had on dilute concentrations. Figure 36 depicts the change in viscosity as a function of the shear rate before and after sulfuric acid addition. The flow curve exhibits a relatively long Newtonian plateau region at moderate shear rates flanked by two shear thinning regions at both low and high shear rates. A decrease in dispersion viscosity after the addition of H_2SO_4 signifies an increase in the electric double layer thickness, which resulted in less nanocrystal interaction than the standard isotropic dispersion. Due to torque limitations, viscosity measurements for samples with excess H_2SO_4 are collected for shear rates greater than 0.215 s^{-1}. No cross-polarized images are presented in Figure 35 as neither micrograph displayed birefringent domains or aggregation.

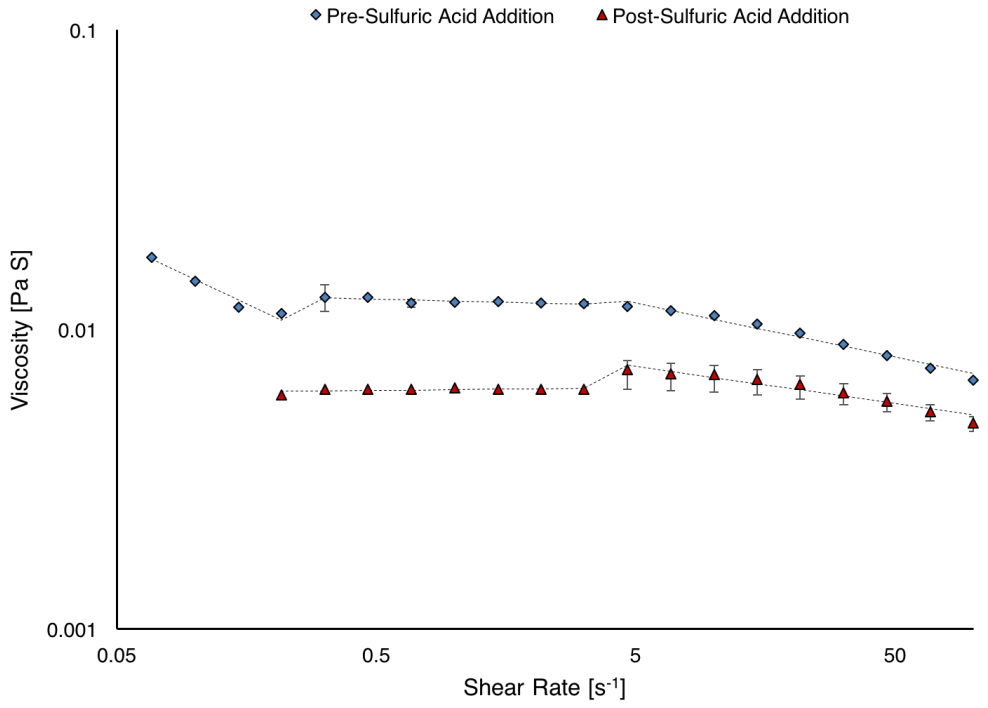

Figure 35 Viscosity as a function of shear rate for 1.89 vol% dispersion samples before and after sulfuric acid addition. The decrease in viscosity suggests an increase in Debye length and decreased nanocrystal interaction. Error bars indicate the minimum and maximum viscosity measurements.

4.6 Counter-Ion Exchange of Cellulose Nanocrystals

The detailed ion exchange protocol that was used in completing the exchange is outlined in Section 3.2 and was adapted from Beck et al. [38]. The initial pH value of ion exchanged CNC was 2.90. Once protonated, the dispersion needed to be concentrated for acid addition and subsequent rheological analysis. Various methods of evaporating excess water were attempted which included the use of orbital shear evaporation at ambient temperature and heating the dispersion to approximately 40˚C under vacuum. In both cases, CNC present in the aqueous dispersions exhibited a propensity to form aggregates. Aggregates in the 5 vol% protonated CNC dispersion, seen in Figure 36, are believed to have formed during the evaporation process as they were visible in the 0.31 vol% protonated sample. These aggregates could be redispersed after vortex mixing for 10 minutes. However, upon adding HCl and H_2SO_4, large flocculated bundles of CNC separated from the dispersion and could not be redispersed without the use of either bath or tip sonication. Sonication can shorten and desulfonate CNC [59] both of which impact CNC phase behavior. Therefore, sonication was not used in this research and the aggregated sample was discarded. Based on Beck et al., it should be possible to obtain aggregate free samples with this procedure, but the protocol was only attempted once due to time constraints. The aggregation problem encountered in this study could be attributed to a low dispersion flowrate through the exchange column or improper dispersion preparation.

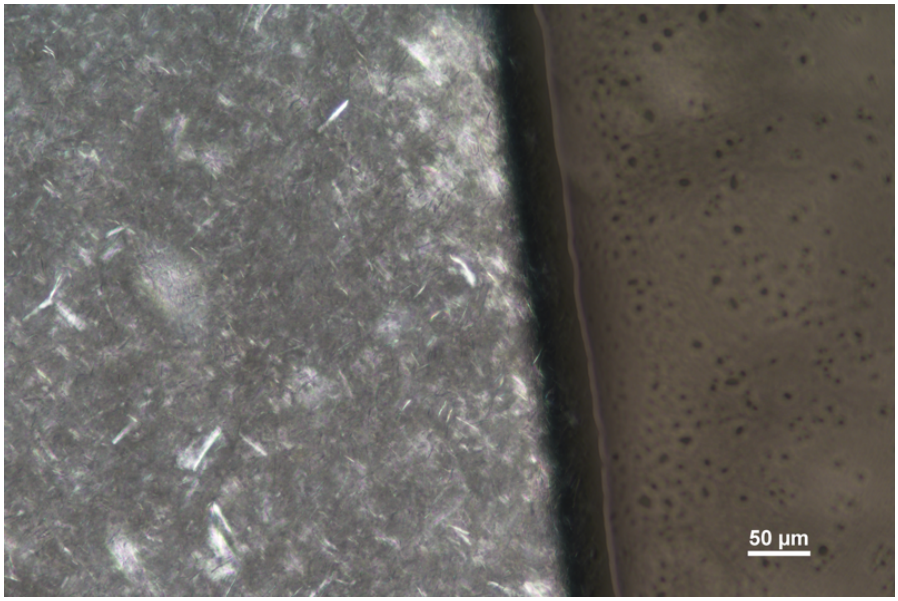

Figure 36 Cross-polarized optical micrograph of 5 vol% protonated CNC dispersion sample. Image taken using LU Plan Fluor 20X objective lens.

4.7 Functionalized Maleic Acid-CNC for Water Resistant Films

To test the hydrophilicity of water resistant CNC films for MEMS applications, water contact angle measurements were collected for maleic acid functionalized CNC films. The results from fluid phase processing of CNC are summarized in Table 4. The process used to functionalize and cross-link CNC delivered lackluster results; some of which include non-uniform films with the minimal cross-linked maleic acid groups and poor water contact angle measurements for a supposedly hydrophobic film. Ultimately, the fluid phase processing through cross-linked maleic acid was abandoned as a potential solution to pursue self-assembled silane monolayer application.

Table 4 Water contact angle results from cross-linked CNC/Maleic acid thin film.

6.7 wt.% CNC-MA Cross-linked	200 μm Wet Thickness	15.5°
	100 μm Wet Thickness	8.47°
3.27 wt.% CNC-MA Cross-linked	200 μm Wet Thickness	9.40°
	100 μm Wet Thickness	9.80°

4.8 Octyltrichlorosilane Self-Assembled Monolayer Formation

Self-assembled monolayers from three types of silane were studied based on their ability to provide reasonably high contact angles over time and ability to remain stable in an aqueous environment. These include octyltrichlorosilane (OTS), octyldecyltrichlorosilane (ODTS), and (3-aminopropyl)triethoxysilane (APTES). Although water contact angle is not indicative of hydrolytic stability, it provides qualitative insight into whether the silane molecules have affected the hydrophilicity of the films. However, due to inconsistencies in data collection, only experiments pertaining to OTS SAM formation is presented.

The protocol utilized in this study was adapted from Ansari (2011) with some alterations made to the reaction time. 250 μL of octyltrichlorosilane was mixed with 50 mL of hexane and allowed to hydrolyze for 45 minutes in a covered glass Petri dish before

coating. Meanwhile, two freestanding CNC films with a thickness of ~3.6 μm were pre-cleaned using a water plasma treatment for 30 seconds to remove any impurities that may be present on the film surface. Once clean, the CNC films were submerged in the OTS solution, place in an ice bath, and allowed to react for 1 hour. Since OTS is a relatively short chain carbon molecule, SAM formation occurs more readily at reduced temperatures [62]. CNC/OTS coated films were then dried in the presence of desiccant overnight.

The result of this monolayer application was a relatively uniform monolayer adsorbed to the surface of the free-standing CNC film. Films had an average initial water contact angle of 107˚ and an average contact angle of 56.4˚ after 30 minutes. Figure 37 depicts CNC/OTS film degradation over time when placed in an aqueous environment. Images were taken using an AmScope boom stand trinocular stereo microscope. In the figure, water propagated through a crack in the film on the left side and migrated to the right; weakening the OTS monolayer from all sides.

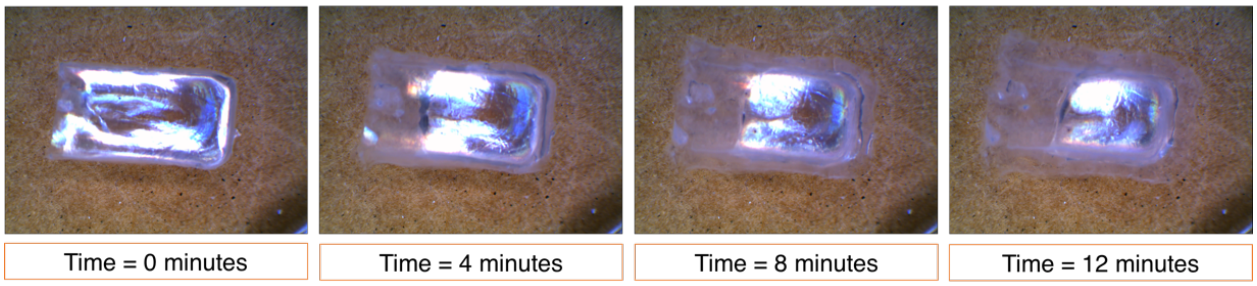

Figure 37 Time lapsed micrographs of OTS coated CNC film degradation.

For comparison, free standing films without OTS coating degraded in less than one minute and exhibited similar propagation of water from the film edge to the center. If OTS were selected for achieving hydrolytically stable CNC MEMS, further optimization of the

SAM application process would need to take place to limit the number of permeation sites. Cross-polarized optical microscopy was taken of an OTS coated, freestanding CNC thin film and appear in Figure 38 below. Protocol amendments could include a slightly extended reaction time, reduced reaction temperature, and slight agitation during the reaction to ensure even exposure to OTS/hexane solution. Alternatively, a different chlorosilane could be used to obtain hydrolytically stable films for MEMS application. Current work by Saha in the Davis/Ashurst group utilizes 3-aminopropyltriethoxysilane (APTES) to achieve hydrolytically stable films and bind to target antigens.

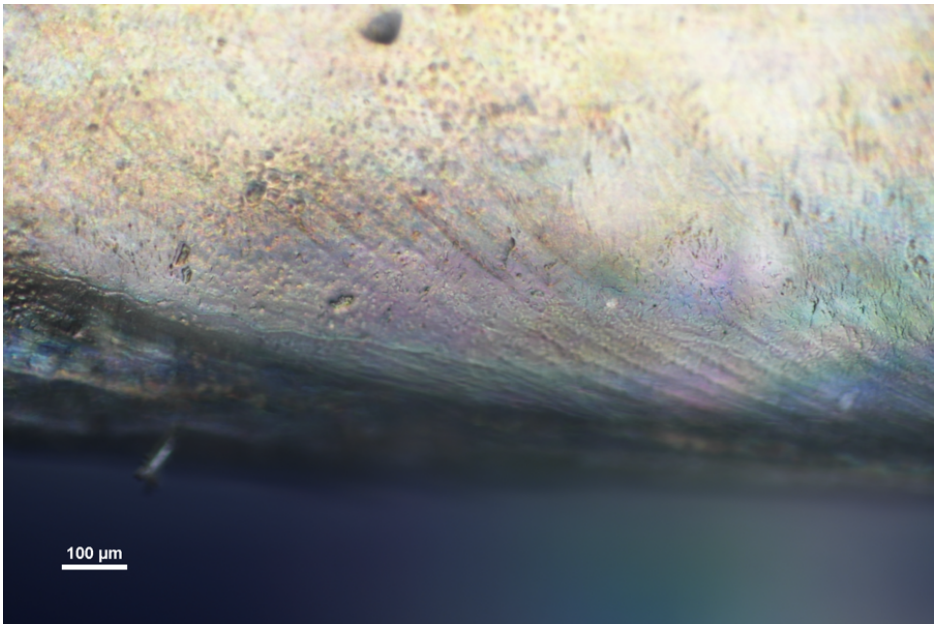

Figure 38 Cross polarized optical micrograph of OTS coated free standing CNC film.

Chapter 5: Conclusions

Cellulose nanocrystals have the potential to positively impact a broad spectrum of consumer goods/industries ranging from biosensing single-use MEMS devices in the biomedical industry to packaging applications in the food industry. It was shown that thin film CNC can be coated with chlorosilane, namely octyltrichlorosilane, to produce water-resistant films that did not degrade in water for 12 minutes. This was monitored using an AmScope trinocular microscope, and degradation time was recorded for half of the sample to disintegrate. This proof of concept experiment highlights the versatility of thin film CNC surface modification and should excite future researchers who seek to optimize the monolayer deposition protocol for their specific application.

As with any new composite or material geared for industrial use via fluid phase processing, there is a need to further refine understanding of CNC dispersions' rheology and phase behavior. Early research was done one CNC made in individual laboratories by a range of methods. The US Forest Products Lab's sulfonated CNC is one of several types available in nearly industrial scale quantities. Rheology is a tool one can use to understand the microstructure of a material and proved to be critical in this study to note changes in the dispersion after the addition of an electrolyte. The present study provides further insight on how ions present in aqueous dispersions of cellulose nanocrystals can affect steady shear rheology at isotropic, anisotropic, and liquid crystalline concentrations. Strongly electronegative ions typically decreased the viscosity of isotropic and liquid crystalline CNC dispersions across all shear rates tested. This trend in dispersion

viscosity after H_2SO_4 addition holds true for the high-end biphasic CNC dispersion (4.48 vol%) as well. In contrast, the low-end biphasic CNC dispersion (3.18 vol%) exhibited an increase in low-shear viscosity and a decrease in viscosity at high shear rates. Moreover, there seemed to be a correlation between the chiral nematic pitch and dispersion viscosity after acid addition, which could potentially be linked to Debye length for modeling dispersion characteristics. Furthermore, the present study could help determine what ions could be added to achieve a desired dispersion viscosity or at what ionic strength a liquid crystalline dispersion would need to be in order to be used in a specific application. Future research should be done to study the impact ionic strength has on dispersion stability and microstructural changes using oscillatory shear rheology.

Works Cited

[1] C. H. Kim, H. J. Youn and H. L. Lee, " Preparation of cross-linked cellulose nanofibril aerogel with water absorbency and shape recovery," *Cellulose,* vol. 22, pp. 3715-3724, 2015.

[2] N. M. A. Ansari, "Understanding the Effect of Surface Topography on Stiction and Friction in MEMS," ProQuest, Ann Arbor, 2011.

[3] D. N. S. Hon, "Cellulose: a Random Walk along Its Historical Path.," *Cellulose,* vol. 1, no. 1, pp. 1-25, 1994.

[4] Y. Habibi, L. Lucia and O. Rojas, "Cellulose Nanocrystals: Chemistry, Self-Assembly, and Applications," *Chemical Reviews,* vol. 110, no. 6, pp. 3479-3500, 04 March 2010.

[5] M. S. Reid, M. Villalobos and E. D. Cranston, "Benchmarking Cellulose Nanocrystals: From the Laboratory to Industrial Production," *Langmuir,* vol. 33, pp. 1583-1598, 2016 December 01.

[6] H. Charreau, M. L. Foresti and A. Vázquez, "Nanocellulose Patents Trends: A Comprehensive Review on Patents on Cellulose Nanocrystals, Microfibrillated and Bacterial Cellulose," *Recent Patents on Nanotechnology,* vol. 7, pp. 56-80, 2013.

[7] X. Wang, C. Yao, F. Wang and Z. Li, "Cellulose-Based Nanomaterials for Energy Applications," *Small,* vol. 13, no. 42, 2017.

[8] M. S. Reid, "Characterizing the Particle-Particle and Particle-Polymer Interactions that Control Cellulose Nanocrystal Dispersion," McMaster University, Hamilton, Ontario, 2017.

[9] M. Kaushik, C. Fraschini, G. Chauve, J.-L. Putaux and A. Moores, "Transmission Electron Microscopy for the Characterization of Cellulose Nanocrystals," *Intech,* pp. 129-163, 2015.

[10] S. Beck-Candanedo, M. Roman and D. G. Gray, "Effect of Reaction Conditions on the Properties and Behavior of Wood Cellulose Nanocrystal Suspensions," *Biomacromolecules,* vol. 6, pp. 1048-1054, 2005.

[11] E. Ureña-Benavides, "Cellulose Nanocrystals Properties and Applications in Renewable Nanocomposites," TigerPrints, Greenville, 2011.

[12] G. J. Vroege and H. N. W. Lekkerkerker, "Phase Transitions in Lyotropic Colloidal and Polymer Liquid Crystals," *Reports on Progress in Physics,* vol. 55, no. 8, pp. 1241-1309, 1992.

[13] Q. Wu, Y. Meng, S. Wang, Y. Li, S. Fu, L. Ma and D. Harper, "Rheological Behavior of Cellulose Nanocrystal Suspension: Influence of Concentration and Aspect Ratio," *Applied Polymer Science,* pp. 1-8, 2014.

[14] G. Friedel, "THE MESOMORPHIC STATES OF MA TTER," *Annales de Physique ,* vol. 18, pp. 273-474, 1922.

[15] A. Donald, A. Windle and S. Hanna, Liquid Crystalline Polymers, Cambridge: Cambridge University Press, 2006.

[16] Dissemination of IT For the Promotion of Materials Science, "Introduction to Anisotropy-Liquid Crystals," University of Cambridge, 2015. [Online]. Available: https://www.doitpoms.ac.uk/tlplib/anisotropy/liquidcrystals.php. [Accessed November 2017].

[17] M. Doi and S. F. Edwards, The Theory of Polymer Dynamics, New York: Oxford University Press, 1986.

[18] V. A. Davis, L. M. Ericson, A. N. G. Parra-Vasquez, H. Fan, Y. Wang, V. Prieto, J. A. Longoria, S. Ramesh, R. K. Saini, C. Kittrell, W. Billups, W. W. Adams, R. H. Hauge, R. E. Smalley and M. Pasquali, "Phase Behavior and Rheology of SWNTs in Superacids," *Macromolecules,* vol. 37, no. 1, pp. 154-160, 2004.

[19] G. Kiss and R. Porter, "Flow induced phenomena of lyotropic polymer liquid crystals: the negative normal force effect and bands perpendicular to shear," in *Mechanical and Thermophysical Properties of Polymer Liquid Crystals. Polymer Liquid Crystals Serie*, vol. 3, Boston, MA: Springer, 1998, pp. 342-350.

[20] K. F. Wissbrun, "Rheology of Rod-like Polymers in the Liquid Crystalline State," *Journal of Rheology,* vol. 25, no. 6, pp. 619-662, 1981.

[21] R. Mezzenga, C. Meyer, C. Servais, A. I. Romoscanu, L. Sagalowicz and R. C. Hayward, "Shear Rheology of Lyotropic Liquid Crystals: A Case Study," *Langmuir,* vol. 21, pp. 3322-3333, 2005.

[22] E. E. Ureña-Benavides, G. Ao, V. A. Davis and C. L. Kitchens, "Rheology and Phase Behavior of Lyotropic Cellulose Nanocrystal Suspensions," *Macromolecules,* pp. 8990-8998, 24 October 2011.

[23] T. Asada, H. Muramatsu, R. Watanabe and S. Onogi, "Rheooptical Studies of Racemic Poly(Γ-Benzyl Glutamate) Liquid-Crystals," *Macromolecules,* vol. 13, no. 4, pp. 867-871, 1980.

[24] A. Montesi, A. A. Peña and M. Pasquali, "Vorticity Alignment and Negative Normal Stresses in Sheared Attractive Emulsions," *Physics Review Letters,* vol. 92, no. 5, pp. 1-4, 2003.

[25] R. Larson, The Structure and Rheology of Complex Fluids., New York, NY: Oxford University Press, 1999.

[26] V. A. Davis, "Phase Behavior and Rheology of Single-Walled Carbon Nanotubes (SWNTs) in Superacids with Application to Fiber Spinning (doctoral dissertation)," ProQuest Information and Learning Company, Houston, 2006.

[27] A. Stroobants, H. Lekkerkerker and T. Odijk, "Effect of Electrostatic Interaction on the Liquid Crystal Phase Transition in Solutions of Rodlike Polyelectrolytes," *Macromolecules,* vol. 19, pp. 2232-2238, 1986.

[28] X. M. Dong, T. Kimura, J.-F. Revol and D. G. Gray, "Effects of Ionic Strength on the Isotropic-Chiral Nematic Phase Transition of Suspensions of Cellulose Crystallites," *Langmuir,* vol. 12, pp. 2076-2082, 1996.

[29] M. Chau, S. E. Sriskandha, D. Pichugin, H. Thérien-Aubin, D. Nykypanchuk, G. Chauve, M. Méthot, J. Bouchard, O. Gang and E. Kumacheva, "Ion-Mediated Gelation of Aqueous Suspensions of Cellulose Nanocrystals," *Biomacromolecules,* vol. 16, pp. 2455-2462, 23 June 2015.

[30] Q. Zuo, T. Lai and P. Huang, "The Effect of the Electric Double Layer on Very Thin Thermal Elastohydrodynamic Lubricating Film," *Tribology Letters,* vol. 45, pp. 455-463, 7 January 2012.

[31] S. Bai, P. Huang, Y. Meng and S. Wen, "Modeling and analysis of interfacial electro-kinetic effects on thin film lubrication," *Tribology International,* vol. 39, pp. 1405-1412, 13 March 2006.

[32] V. K. Varadan, K. Vinoy and K. Jose, "Microelectromechanical Systems (MEMS) and Radio Frequency MEMS," in *RF MEMS*, Chichester, John Wiley & Sons, 2003.

[33] P. Podsiadlo, S.-Y. Choi, B. Shim, J. Lee, M. Cuddihy and N. A. Kotov, "Molecularly Engineered Nanocomposites: A Layer-by-Layer Assembly of Cellulose Nanocrystals," *Biomacromolecules,* vol. 6, pp. 2914-2918, 2005.

[34] J. Dolbow and M. Gosz, "Effect of out-of-plane properties of a polyimide film on the stress fields in microelectronic structures," *Mechanics of Materials,* vol. 23, pp. 311-321, 1996.

[35] A. Ulman, "Formation and Structure of Self-Assembled Monolayers," *Chemical Reviews,* vol. 96, pp. 1533-1554, 1996.

[36] The Process Development Center, "Cellulose Nanomaterials," University of Maine, [Online]. Available: umaine.edu/pdc/cellulose-nano-crystals/. [Accessed September 2017].

[37] H. Oguzlu, C. Danumah and Y. Boluk, "Colloidal behavior of aqueous cellulose nanocrystal suspensions," *Current Opnion in Colloid & Interface Science,* vol. 29, pp. 46-56, 2017.

[38] S. Beck, M. Méthot and J. Bouchard, "General Procedure for Determining Cellulose Nanocrystal Sulfate Half-Ester Content by Conductometric Titration," *Cellulose,* vol. 22, pp. 101-116, 2015.

[39] X. M. Dong, J.-F. Revol and D. G. Gray, "Effect of Microcrystallite Preparation Conditions on the Formation of Colloid Crystals of Cellulose," *Cellulose,* vol. 5, pp. 19-32, 1998.

[40] A. D. Haywood, "Flow-Directed Assembly of Cellulose Nanocrystal Dispersions with Ordered Film Applications," Auburn University, Auburn, 2016.

[41] P. C. Robinson and M. W. Davidson, "Polarized Light Microscopy," Nikon, [Online]. Available: https://www.microscopyu.com/techniques/polarized-light/polarized-light-microscopy. [Accessed 2017].

[42] D. B. Murphy, K. R. Spring, T. J. Fellers and M. W. Davidson, "Principles of Birefringence," Nikon, 2017. [Online]. Available: https://www.microscopyu.com/techniques/polarized-light/principles-of-birefringence. [Accessed October 2017].

[43] C. W. Macosko, Rheology: Principles, Measurements, and Applications, Wiley, 1994.

[44] G. Ao, "Liquid Crystalline Phase Behavior of Double-Stranded DNA Stabilized Single-Walled Carbon Nanotubes Dispersions," Auburn University, 2010.

[45] "Conductivity Theory and Technical Tips," Cole Parmer, 16 March 2017. [Online]. Available: www.coleparmer.com/tech-article/conductivity. [Accessed November 2017].

[46] A. Cassie, "Contact Angles," *Discussions of the Faraday Society,* vol. 44, pp. 11-16, 1948.

[47] D. Kwok and A. Neumann, "Contact Angle Measurement and Contact Angle Interpretation," *Advances in Colloid and Interface Science,* vol. 81, pp. 167-249, 1999.

[48] J. Sanchez-Reyes and L. A. Archer, "Interfacial Slip Violations in Polymer Solutions: Role of Microscale Surface Roughness," *Lanmuir,* vol. 19, pp. 3304-3312, 01 03 2003.

[49] L. Feng, S. Li, Y. Li, H. Li, L. Zhang, J. Zhai, Y. Song, B. Liu, L. Jiang and D. Zhu, "Super-Hydrophobic Surfaces: From Natural to Artificial," *Advanced Materials,* vol. 14, no. 2, 17 December 2002.

[50] A. D. Haywood and V. A. Davis, "Effects of liquid crystalline and shear alignment on the optical properties of cellulose nanocrystal films," *Cellulose,* no. 24, pp. 705-716, 2016 December 16.

[51] A. D. Haywood, K. M. Weigandt, P. Saha, M. Noor, M. J. Green and V. A. Davis, "New insights into the flow and microstructural relaxation behavior of biphasic cellulose nanocrystal dispersions from RheoSANS," *Soft Matter,* vol. 13, pp. 8451-8462, 2017.

[52] G. Ao, D. Nepal and V. A. Davis, "Rheology of lyotropic cholesteric liquid crystal forming single-wall carbon nanotube dispersions stabilized by double-stranded DNA," *Rheologica Acta,* vol. 55, no. 9, pp. 717-725, September 2016.

[53] J. Goswami and V. A. Davis, "Viscoelasticity of Single-Walled Carbon Nanotubes in Unsaturated Polyester Resin: Effects of Purity and Chirality Distribution," *Macromolecules,* vol. 48, pp. 8641-8650, 2015.

[54] T. Xu and V. A. Davis, " Rheology and Shear-Induced Textures of Silver Nanowire Lyotropic Liquid Crystals," *Journal of Nanomaterials,* vol. 2015, pp. 1-9, 2015.

[55] T. Xu and V. A. Davis, "Liquid Crystalline Phase Behavior of Silica Nanorods in Dimethyl Sulfoxide and Water," *Langmuir,* vol. 30, pp. 4806-4813, 2014.

[56] E. E. Ureña-Benavides, M. J. Kayatin and V. A. Davis, "Dispersion and Rheology of Multiwalled Carbon Nanotubes in Unsaturated Polyester Resin," *Macromolecules,* vol. 46, no. 4, pp. 1642-1650, 2013.

[57] G. Ao, D. Nepal, M. Aono and V. A. Davis, "Cholesteric and Nematic Liquid Crystalline Phase Behavior of Double- Stranded DNA Stabilized Single- Walled Carbon Nanotube Dispersions," *ACS Nano,* vol. 5, no. 2, pp. 1450-1458, 2001.

[58] M. J. Kayatin and V. A. Davis, "Viscoelasticity and Shear Stability of Single-Walled Carbon Nanotube/Unsaturated Polyester Resin Dispersions," *Macromolecules,* vol. 42, no. 17, pp. 6624-6632, 2009.

[59] S. Shafiei-Sabet, W. Y. Hamad and S. G. Hatzikiriakos, "Rheology of Nanocrystalline Cellulose Aqueous Suspensions," *Langmuir,* vol. 28, pp. 17124-17133, 2012.

[60] S. Shafiei-Sabet, W. Hamad and S. Hatzikiriakos, "Ionic strength effects on the microstructure and shear rheology of cellulose nanocrystal suspensions," *Cellulose,* vol. 21, pp. 3347-3359, 21 August 2014.

[61] J. Pan, W. Hamad and S. Straus, "Parameters Affecting the Chiral Nematic Phase of Nanocrystalline Cellulose Films," *Macromolecules,* vol. 43, pp. 3851-3858, 2010.

[62] D. Aswal, S. Lenfant, D. Guerin and D. Vuillaume, "Self assembled monolayers on silicon for molecular electronics," *Elsevier,* 2005.

[63] V. A. Davis, "Liquid Crystalline Assembly of Nanocylinders," *Journal of Materials Research,* vol. 26, no. 2, pp. 140-153, 2011.

[64] M. Doi and S. F. Edwards, The Theory of Polymer Dynamics.

[65] Cole Parmer, "Conductivty Theory and Technical Tips," 16 March 2017. [Online]. Available: www.coleparmer.com/tech-article/conductivity. [Accessed November 2017].